Received: 30 June 2022 | Revised: 11 October 2022 | Accepted: 30 October 2022

DOI: 10.1002/nbm.4864

RESEARCH ARTICLE

NMR IN BIOMEDICINE WILEY

Efficient performance analysis and optimization of transient-state sequences for multiparametric magnetic resonance imaging

Miha Fuderer | Oscar van der Heide | Hongyan Liu | Cornelis A. T. van den Berg | Alessandro Sbrizzi

Radiotherapy, Imaging Division, University Medical Center Utrecht, Utrecht, the Netherlands

Correspondence
Miha Fuderer, Radiotherapy, Imaging Division, University Medical Center Utrecht, 3584CX Utrecht, the Netherlands.
Email: m.fuderer@umcutrecht.nl

Funding information
Nederlandse Organisatie voor Wetenschappelijk Onderzoek (NWO), Grant/Award Number: 17986

Abstract

In transient-state multiparametric MRI sequences such as Magnetic Resonance Spin TomogrAphy in Time-domain (MR-STAT), MR fingerprinting, or hybrid-state imaging, the flip angle pattern of the RF excitation varies over the sequence. This gives considerable freedom to choose an optimal pattern of flip angles. For pragmatic reasons, most optimization methodologies choose for a single-voxel approach (i.e., without taking the spatial encoding scheme into account). Particularly in MR-STAT, the context of spatial encoding is important. In the current study, we present a methodology, called BLock Analysis of a K-space-domain Jacobian (BLAKJac), which is sufficiently fast to optimize a sequence in the context of a predetermined phase-encoding pattern. Based on MR-STAT acquisitions and reconstructions, we show that sequences optimized using BLAKJac are more reliable in terms of actually achieved precision than conventional single-voxel–optimized sequences. In addition, BLAKJac provides analytical tools that give insights into the performance of the sequence in a very limited computation time. Our experiments are based on MR-STAT, but the theory is equally valid for other transient-state multiparametric methods.

KEYWORDS
evaluation and performance, magnetic resonance imaging, optimizationquantification and estimation

1 | INTRODUCTION

Many MR techniques acquire qualitative images that are "weighted" by tissue properties like T_1 or T_2. Typically, these are steady-state acquisition techniques, allowing for simple reconstruction paradigms. By combining multiple steady-state acquisitions, quantitative information regarding several tissue properties can be extracted.[1–11] However, these steady-state approaches require a multiplicity of scans or scan-segments, leading to scan times that are too long for clinical practice. Transient-state sequences may overcome this downside.

Abbreviations used: BLAKJac, BLock Analysis of a K-space-domain Jacobian; CRLB, Cramér–Rao lower bound; MRF, magnetic resonance fingerprinting; MR-STAT, Magnetic Resonance Spin TomogrAphy in Time-domain; RF, radio frequency.

Examples of transient-state sequences are MR fingerprinting (MRF),[12,13] Magnetic Resonance Spin TomogrAphy in Time-domain (MR-STAT),[14,15] or transient/hybrid-state imaging. Transient-state sequences have the promise of more efficiently deducing several tissue properties from one single scan. In order to achieve that, these techniques abandon the steady-state approach and introduce time-varying sequence parameters (e.g., the radio-frequency [RF] flip angle). These techniques trade simplicity for efficiency, where "efficiency" is seen as obtaining more information (low noise or artifacts, high resolution) per unit time – or, conversely, faster acquisition without the loss of accuracy or precision.

However, transient-state techniques come with a cost. Optimizing a typical MR-STAT or MRF sequence requires choosing hundreds or thousands of different flip-angle values, while a steady-state sequence requires to optimize only one. The optimization of flip-angle trains is addressed in.[16–30] Most of this work, in particular refs,[16–21,26,28,29] is limited to single-voxel optimization, in the sense that it does not take the encoding pattern into account when optimizing the RF flip angle pattern.

When focusing on the inherent performance potential of a sequence, rather than on the deficiency of the reconstruction process, the Cramér–Rao lower bound (CRLB) is the most appropriate tool. The CRLB has been used for single-voxel optimization.[16,17,20,26] Similarly, Byanju et al.[27] focus exclusively on low spatial frequencies, bringing it close to single-voxel, while Leitão et al.[28] assume full sampling at every instant, also turning the optimization into a single-voxel approach. Other work[22–24] analyzes the efficiency in the context of the encoding pattern and focuses on the undersampling artefacts obtained by the specific reconstruction process; that work does not apply the CRLB. Also, Jordan et al.[30] take encoding into account but choose not to apply CRLB as a criterion. Up-to-date application of the CRLB in the context of a RF time-varying train combined with gradient encoding has not been presented before.

In our approach, we take the spatial encoding-pattern into account – and we focus on the theoretical CRLB, which we study by means of the Jacobian and its associated Fisher Information Matrix. This is a large matrix, of the order of $n \times n$; in non-Cartesian sequences, n is the number of samples in k-space; in Cartesian sequences, it is the number of different phase-encoding values (in our MR-STAT examples, $n = 224$). A full inversion of a matrix of that size incurs a prohibitive processing burden. In this paper, we present a solution that is both fast and useful.

As a solution, we propose a methodology that factorizes the Jacobian, a methodology called BLock Analysis of a K-space-domain Jacobian (BLAKJac) (see Section 2). BLAKJac is fast relative to a full inversion because it achieves an n^2 factor in performance increase in the analysis of sequences. This allows for iterative sequence optimization in the context of encoding with a total computing time of the order of minutes. As one useful feature of BLAKJac, we show, on a Cartesian-encoded sequence reconstructed by MR-STAT,[31] that sequences optimized in the context of spatial encoding (2D) reliably predict the precision of T_1- or T_2-maps, as opposed to single-voxel (0D) optimized sequences. As another useful feature, BLAKJac allows for prospective analysis of spatial noise spectra in the obtainable tissue parameter maps. Given any sequence of time-varying flip angles and gradient-encoding patterns, it can predict and visualize which spatial frequencies will be most affected by noise, as shown in the simulations and experimental tests.

2 | THEORY

To evaluate the performance of a sequence, it is necessary to evaluate the inverse of the Fisher Information Matrix $J^H J$, where J is the Jacobian of the associated signal model. In order to allow efficient inversion of the information matrix, we propose a factorization of the Jacobian based on the following idea (see also Figure 1): we focus on the spatial *frequency* domain and consider thus the *Fourier transforms* of properly scaled parameter maps (see Equation 2). These transformed maps are denoted as "auxiliary variables" with the symbol "f" in the sequel. Note that we do not need to actually calculate f as an intermediate step: this notion only serves to explain the factorization of the Jacobian.

Thus, we consider the composite signal model $\boldsymbol{\Gamma} = h(f(\boldsymbol{u}))$ for a given function h, where $h \circ f = \Gamma$. This leads to a splitting of the Jacobian into two factors: $\boldsymbol{J}_{\Gamma/\mathrm{u}} = \boldsymbol{J}_{\Gamma/\mathrm{f}} \boldsymbol{J}_{\mathrm{f/u}}$, where each of these two factors leads to a computationally efficient inversion of the information matrix.

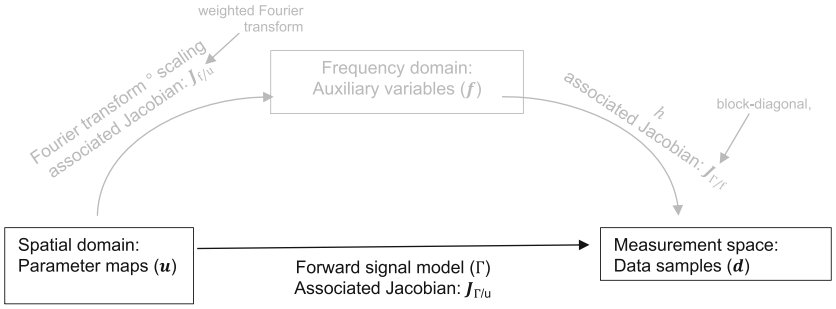

FIGURE 1 Proposed signal model decomposition and associated Jacobian factors. The arrows represent mappings, not processing steps. The introduction of the auxiliary variables f allows to factorize the Jacobian into two factors, $\boldsymbol{J}_{\mathrm{f/u}}$ and $\boldsymbol{J}_{\Gamma/\mathrm{f}}$; both can be efficiently evaluated

(Here, $\mathbf{\Gamma}$ is the signal model, see also Equation (A1) in Appendix A.1; $\boldsymbol{u}$ is the set of unknowns [e.g., the T_1 and T_2 values at all locations]; and h and f are arbitrary functions. A symbol like $\boldsymbol{J}_{f/u}$ represents the Jacobian of f with respect to u, that is, the matrix $\left[\frac{\partial f(\boldsymbol{u})}{\partial \boldsymbol{u}}\right]$).

This section is structured as follows: subsection 2.1 links the CRLB to the Fisher Information Matrix. Subsection 2.2 elaborates on the truncated Taylor expansion of the forward model, which is essential to show that $\boldsymbol{J}_{\Gamma/f}$ can be approximated as a block-diagonal; this property delivers the speedup of the computations. Subsection 2.3 elaborates on the applications of this approach.

2.1 | CRLB for spatially dependent parameter maps

Transient-state multiparametric MRI sequences are often used to estimate tissue properties like T_1, T_2, or proton density.[12–16,32] For reconstruction techniques that are unbiased, there is a theoretical limit on the uncertainty to the resulting parameter maps, namely, the CRLB:

$$E\left[(\boldsymbol{u}-\widehat{\boldsymbol{u}})(\boldsymbol{u}-\widehat{\boldsymbol{u}})^H\right] \succeq \boldsymbol{I}^{-1}(\boldsymbol{u}). \tag{1}$$

Here, "$E[\ ]$" means "expectation value", $\boldsymbol{u}$ denotes the vector of unknowns, and $\widehat{\boldsymbol{u}}$ is an unbiased estimator thereof. "H" denotes the Hermitian conjugate and $\boldsymbol{I}$ is the Fisher Information Matrix.

To evaluate the Fisher Information Matrix, we assume that we have a perfect forward MR signal model $\Gamma(.)$ that exactly models spin dynamics and sequence-design settings, leading to sampled data. We also assume that this data is only confounded by independent and identically distributed (i.i.d.) thermal noise with variance σ^2. In that case, $\boldsymbol{I}(\boldsymbol{u})$ reduces to $\frac{1}{\sigma^2}\boldsymbol{J}^H_{\Gamma/u}\boldsymbol{J}_{\Gamma/u}$. Here, the notation $\boldsymbol{J}_{\Gamma/u}$ is the Jacobian matrix $\left[\frac{\partial \Gamma(\boldsymbol{u})}{\partial \boldsymbol{u}.}\right]$.

Note the similarity in formalism to, for example, the work by Zhao et al.[17]; the fundamental difference is that Zhao et al.[17] consider the vector of unknowns to consist of just N_p elements, with N_p the number of properties (e.g., three), thereby defining $\boldsymbol{u} = [T_1, T_2, M_0]^T$ (with M_0 representing the proton density). In our work, $\boldsymbol{u}$ is a vector of $N_p N_{\text{locations}}$ elements, which thus represents the whole spatial distribution of each parameter type.

In the sequel, the symbol $\boldsymbol{r}$ will denote a three-elements location vector (of which there are $N_{\text{locations}}$ [i.e., the number of voxels]); because we assume that the set of locations spans a Cartesian grid, we apply a slight notational abuse and use $\boldsymbol{r}$ also as an index to u (i.e., the full vector $\boldsymbol{u}$ consists of elements $u_{p,\boldsymbol{r}}$). Similarly, the k-space vector $\boldsymbol{k} = (k_x, k_y, k_z)$ will also be used as an index having N_k distinct values. Here, we take $N_k = N_{\text{locations}}$.

For any flip-angle and gradient-encoding scheme, we can calculate $\boldsymbol{J}_{\Gamma/u}$, from which the expected noise statistics in the reconstructed parameters can be calculated by the inversion of $\boldsymbol{J}^H_{\Gamma/u}\boldsymbol{J}_{\Gamma/u}$. Yet, in practice, this inversion is problematic. This Fisher Information Matrix has size $N_pN_k \times N_pN_k$; the inversion of a full matrix of this size requires $O\left(N_k^3 N_p^3\right)$ operations. A factorization of the Jacobian, elaborated below, allows for a substantial speedup of the aforementioned inversion problem.

2.2 | Taylor expansion of the model Γ and factorization of the Jacobian

Appendix A elaborates on a Taylor expansion of the signal model $\Gamma(.)$, which allows for a factorization of the Jacobian. That formalism is based on a first-order Taylor approximation of the Bloch model, that is, on $G_{(\boldsymbol{k},\,i)}\left(u_{1,\boldsymbol{r}}, \ldots, u_{(N_p-1),\boldsymbol{r}}\right) \approx g_{(\boldsymbol{k},\,i)} + \sum_{p=1}^{N_p-1}\left[\frac{\partial G_{(\boldsymbol{k},\,i)}}{\partial u_p}\Big|_{\boldsymbol{u}=\boldsymbol{u}^{\text{ref}}} \cdot \left(u_{p,\boldsymbol{r}} - u_p^{\text{ref}}\right)\right]$, where G is the Bloch signal model at timepoint $(\boldsymbol{k}, i)$ given the relaxation properties $u_{1,\boldsymbol{r}},\ldots,u_{(N_p-1),\boldsymbol{r}}$ at any location $\boldsymbol{r}$; a derivative like $\frac{\partial G_{(\boldsymbol{k},\,i)}}{\partial u_1}\Big|_{\boldsymbol{u}=\boldsymbol{u}^{\text{ref}}}$ can be seen as "the level of T1-weighting" at time point $(\boldsymbol{k}, i)$. The values, u_p^{ref}, with $p = 1,\ldots,N_p - 1$, are arbitrary reference values that are chosen to be constant over the whole volume.

The aforementioned factorization separates the (weighted) Fourier-transform component from the Jacobian, the "remaining" factor being close to a block-diagonal matrix. More precisely, we define auxiliary variables as

$$\begin{aligned} f_{0,\boldsymbol{k}} &= \mathcal{F}(\boldsymbol{u}_0)_{\boldsymbol{k}} \\ f_{(p\geq 1),\boldsymbol{k}} &= \mathcal{F}\left(\boldsymbol{u}_0 \odot \left(\frac{\boldsymbol{u}_p}{u_p^{\text{ref}}} - \boldsymbol{1}\right)\right)_{\boldsymbol{k}}, \end{aligned} \tag{2}$$

where "$\odot$" is the Hadamard product and $\mathcal{F}(\cdot)$ is shorthand for n-dimensional Fourier transform (i.e., $\mathcal{F}(\boldsymbol{x})_{\boldsymbol{k}} = \sum_{\boldsymbol{r}} x_{\boldsymbol{r}} e^{i2\pi \boldsymbol{k}\cdot\boldsymbol{r}}$); as already mentioned, the vector $\boldsymbol{k} = (k_x, k_y, k_z)$ is also used as an index, similarly to vector $\boldsymbol{r}$. While $\boldsymbol{f}_0$ represents the Fourier transform of the proton-density map, the physical meaning of, for example, $\boldsymbol{f}_1$, can be seen as the Fourier transform of a weighted T1 map.

Using these auxiliary variables, we consider the signal model as $\mathbf{\Gamma} = h(f(\boldsymbol{u}))$ (see Figure 1). We thereby split the Jacobian into two factors: $\boldsymbol{J}_{\Gamma/u} = \boldsymbol{J}_{\Gamma/f}\boldsymbol{J}_{f/u}$, where

- The factor $\boldsymbol{J}_{\Gamma/\mathrm{f}}$ is approximated as a block-diagonal. This diagonal structure is shown in Figure 2.
- The factor $\boldsymbol{J}_{\mathrm{f/u}}$ is a weighted Fourier transform matrix, with well-known noise properties, $\sigma_p^2 \propto \sum_{\boldsymbol{k}} \left(\left(\boldsymbol{J}_{\Gamma/\mathrm{f}}^H \boldsymbol{J}_{\Gamma/\mathrm{f}} \right)^{-1} \right)_{(\boldsymbol{k},\, p),(\boldsymbol{k},\, p)}$; here, σ_p is the Cramér–Rao lower limit to the standard deviation of the reconstructed noise in property p (e.g., the T_1-map). The proportionality factor in the formula above includes the choice of u_p^{ref}, the noise level in the data (σ), as well as the proton density.

Note that $\boldsymbol{J}_{\Gamma/\mathrm{f}}$ is close to being a block-diagonal, while the original $\boldsymbol{J}_{\Gamma/\mathrm{u}}$ is not. This is a crucial aspect because it allows for the N_k^2 efficiency factor when inverting the Fisher Information Matrix. The resulting performance gain is particularly beneficial if the inversion $\left(\boldsymbol{J}_{\Gamma/\mathrm{f}}^H \boldsymbol{J}_{\Gamma/\mathrm{f}} \right)^{-1}$ needs to be evaluated multiple times, for instance, during an iterative optimization process.

2.3 | Analysis and applications of BLAKJac

The proposed BLAKJac factorization allows for several useful applications, among which are noise spectrum analysis and sequence optimization.

2.3.1 | BLAKJac for noise spectrum analysis

BLAKJac can efficiently predict the noise spectrum in the reconstructed parameter maps $\boldsymbol{u}$. Assuming an i.i.d. noise at the input, the noise covariance matrix at the auxiliary variables $\boldsymbol{f}$ is approximated by $\sigma^2 \left(\boldsymbol{J}_{\Gamma/\mathrm{f}}^H \boldsymbol{J}_{\Gamma/\mathrm{f}} \right)^{-1}$. By examining the resulting noise variance on a given property p and a measurement sequence, we can extract an $N_k \times N_k$ submatrix, $\left[\sigma^2 \left(\boldsymbol{J}_{\Gamma/\mathrm{f}}^H \boldsymbol{J}_{\Gamma/\mathrm{f}} \right)^{-1} \right]_{pp}$. Given the block-diagonality of $\boldsymbol{J}_{\Gamma/\mathrm{f}}$, this submatrix is diagonal.

Consequently, BLAKJac provides the information on the noise variance as a function of spatial frequency, as will be shown in the numerical and experimental tests (Figures 10 and 11, details will follow).

2.3.2 | BLAKJac for sequence optimization

Because the Jacobian $\boldsymbol{J}_{\mathrm{f/u}}$ is in essence a Fourier transform matrix, the noise variance in $\boldsymbol{u}_p$ can be obtained by a sum of the variances of its k-space components. Symbolically,

$$\sigma_p^2 \propto \sum_{\boldsymbol{k}} \left(\left(\boldsymbol{J}_{\Gamma/\mathrm{f}}^H \boldsymbol{J}_{\Gamma/\mathrm{f}} \right)^{-1} \right)_{(\boldsymbol{k},\, \boldsymbol{p}),(\boldsymbol{k},\, p)}, \tag{3}$$

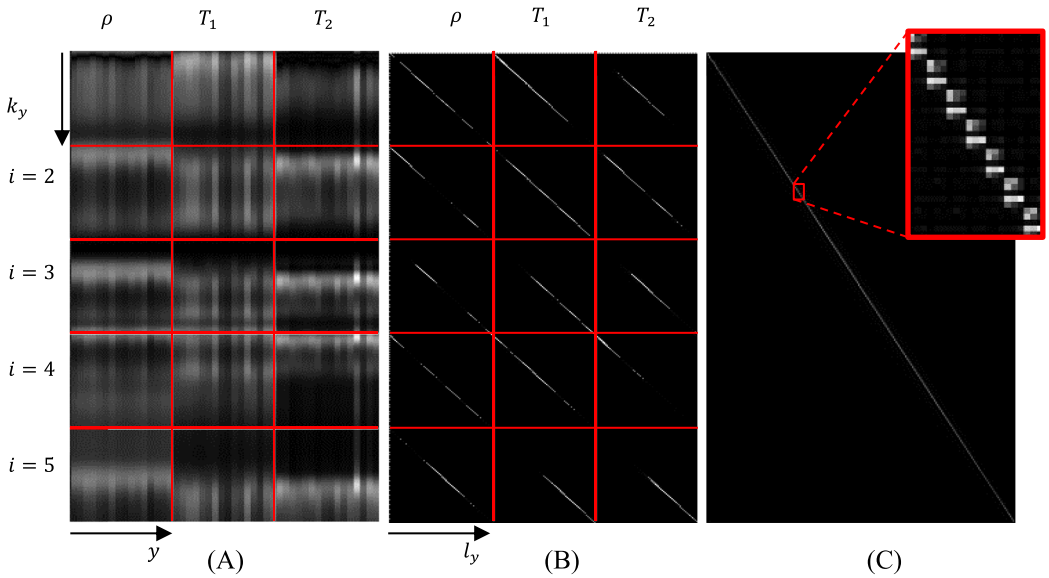

FIGURE 2 Graphical representation of the absolute values of the elements of the Jacobian matrix in a Cartesian case (where k_x is not relevant, so $\boldsymbol{k}$ reduces to k_y). (A) $\boldsymbol{J}_{\Gamma/\mathrm{u}}$, (B) The matrix $\boldsymbol{J}_{\Gamma/\mathrm{f}}$. Part (C) shows the same content as (B), but with the indices rearranged so that the instance i and the property p are the inner indices, while $\boldsymbol{k}$ and $\boldsymbol{l}$ are the outer indices. Part (C) demonstrates that the 224 diagonal blocks, $\boldsymbol{k} = \boldsymbol{l}$, are dominant. In the example, the blocks have a size of 5×3. The black color corresponds to 0

with σ_p the expected standard deviation to the map of property p (e.g., the T_1-map).

From the values of σ_p, we can calculate an overall figure of merit C as $C = \frac{1}{N_p}\sum_p \frac{\sigma_p}{u_p^{\text{ref}}}$ or as $C = \max\left(\frac{\sigma_p}{u_p^{\text{ref}}}\right)$. Optimal sequences can be obtained by minimizing C. This is elaborated in section 3.2.

Our approach also allows to map the performance of a sequence over a (T_1, T_2)-landscape, thereby highlighting potentially suboptimal encoding for specific values of (T_1, T_2) (Figure 3).

3 | METHODS

3.1 | Details of the applied MR-STAT sequence

In all our experiments, we applied Cartesian MR-STAT measurements.[15] An MR-STAT sequence, as shown in Figure 4C, consists of a repeated acquisition ($T_R = 10$ ms) of single lines through k-space; T_R as well as the total gradient area between pulses is held constant (a.k.a. steady-state free precession), while the flip angle is varied from pulse to pulse. Experiments were performed on a Philips Achieva 3T system with a 13-element head coil (but precombined into a single virtual coil for our experiments, by taking the first principal component of the concatenated coil signals). In all experiments, we measured a single slice with 4-mm thickness. The scan parameters were $T_E = 5$ ms with a voxel size of 1 mm × 1 mm, $N_{k_y} = N_{k_x} = 224$, field of view = $(224\text{mm})^2$, and no parallel imaging. A sequence is always preceded by a single adiabatic inversion pulse.

3.2 | Sequence optimization

We used BLAKJac to calculate and minimize a figure of merit C given a time-varying sequence of 1120 flip angles. According to eqn. A2 in Sbrizzi et al.,[31] a choice of $C = \max_{p \in \{T_1, T_2\}}\left(\frac{\sigma_p}{u_p^{\text{ref}}}\right)$ was applied.

As explained in the Theory section, σ_p is calculated by inverting the Fisher Information Matrix. The inversion requires $O\left(N_k N_p^3\right)$ operations. In general, N_k is of the same order as $N_{\text{locations}}$, which in our example was 224^2; furthermore, we applied $N_p = 3$ (proton density, T_1, and T_2). If we consider Cartesian sequences and we neglect the relaxation during a readout line, then all samples of that readout line share the same flip angle history, thus they share the same $\boldsymbol{J}_{\Gamma/f}$. In that situation, the inversion of the Fisher Information Matrix requires only $O\left(N_{\text{phase-encodings}} N_p^3\right)$ operations, which in our example was of the order of $224 \cdot 3^3$. Given the compact block-diagonal representation of BLAKJac, the processing time is dominated by the evaluation of the Jacobian for all 1120 timepoints (i.e., by evaluating the entries $\left[\frac{\partial G_{(k,\,i)}}{\partial u_p}\Big|_{\boldsymbol{u}=\boldsymbol{u}_{\text{ref}}}\right]$, referring to Appendix A1). This evaluation can be performed efficiently using a finite-difference method based on Extended Phase Graphs.[33] In practice, the evaluation and inversion of the Fisher Information Matrix required approximately 10 ms on a single-core Intel Xeon CPU E5–1620 v3 running at 3.50 GHz.

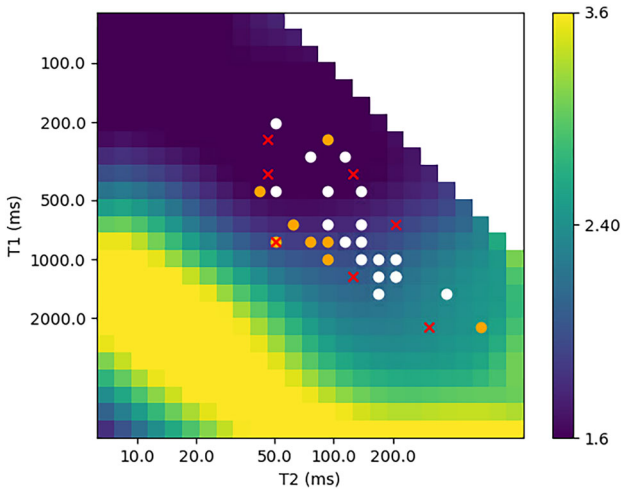

FIGURE 3 A map of $C = \frac{1}{N_p}\sum_{p \in \{\rho,\, T_1,\, T_2\}}\left(\frac{\sigma_p}{u_p^{\text{ref}}}\right)$ (logarithmic color scale) over a range of (T_1, T_2) for the sequence called "2D-best" (see section 3.2). The red crosses indicate the set of $\left(T_1^{\text{ref}}, T_2^{\text{ref}}\right)$ considered during the optimization. The orange dots roughly indicate a set of human tissues (gray matter, white matter, muscle, liver, kidney, lung, CSF, fat) and the white dots the gel-filled vials of the Eurospin phantom. The figure shows that the criterion depends on the actual (T_1, T_2) and it shows that—in the relevant areas—this function is smoothly varying. CSF, cerebrospinal fluid

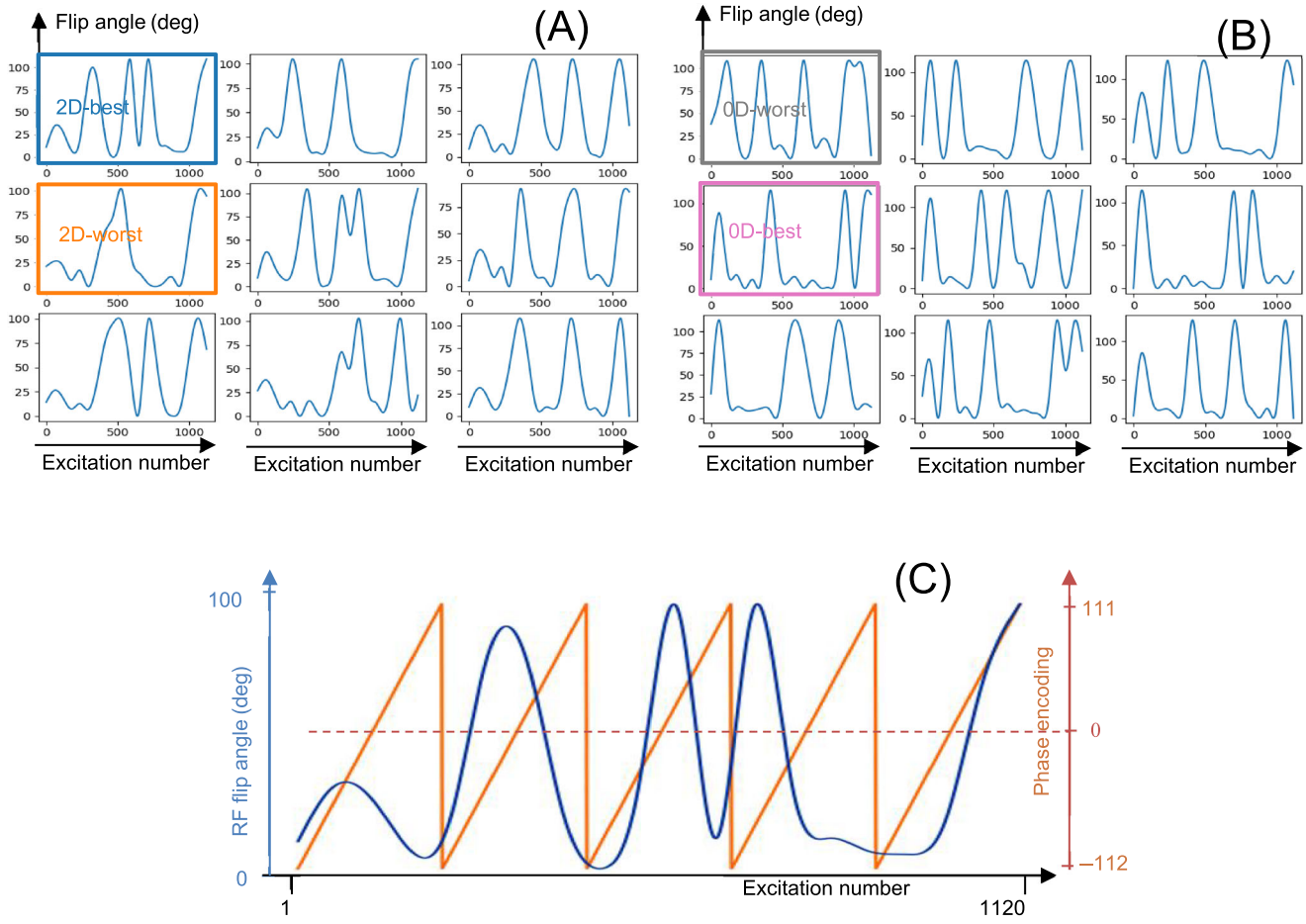

FIGURE 4 (A) Sequences generated in the context of phase-encoding and (B) Single-voxel–optimized sequences. Flip angle (in degrees) is vertical, time is horizontal. For each approach, nine optimizations were done with different randomized starting patterns (see text). Frame colors correspond to colors used in subsequent graphs; "best" and "worst" refer to the performance in a 2D setting. Part (C) is, enlarged, the first sequence of (A), including a representation of the phase-encoding pattern. A sweep of 224 phase-encoding values is repeated five times, so the acquisition time of the whole sequence is $(224 \cdot 5) \cdot 10\,\text{ms} = 11.2\,\text{s}$

The performance metric C depends on the exact values of u^{ref}, that is, the chosen T_1^{ref} and T_2^{ref} values. This dependence is not very strong, as shown by the smoothness of the figure of merit function in Figure 3. Nevertheless, there is a non-negligible variation of $\mathcal{C}$ over the clinically relevant range of (T_1, T_2) (see the orange dots). For that reason, we chose to evaluate the optimization criterion over a multiplicity of reference points. In detail, we chose $N_{\text{combinations}} = 7$ different combinations of $\left(T_1^{\text{ref}}, T_2^{\text{ref}}\right)$ (see the red crosses in Figure 3); these are spanning the range of relaxation values of frequently occurring human tissues. The combined criterion was taken as an average over the outcomes:

$$\overline{C}(\mathcal{S}) = \frac{1}{N_{\text{combinations}}} \sum_{i=1}^{N_{\text{combinations}}} C\left(\mathcal{S}; \left(T_1^{\text{ref}}, T_2^{\text{ref}}\right)_i\right). \tag{4}$$

In principle, $\mathcal{S}$ refers to all the relevant sequence settings, but in the sequel we will only consider the time-varying RF flip angles as being variable in time and consider all the other parameters as being constant. Consequently, approximately 70 ms was needed to evaluate $\overline{C}(\mathcal{S})$ given a sequence $\mathcal{S}$ of 1120 time points.

Referring to Equation (3), and as motivated in the Discussion section, we slightly modify the estimation of σ_p by weighing the 10 lowest spatial frequencies with a higher factor (3.0) than all other spatial frequencies.

Using the Nelder–Mead algorithm[34] from the Optim.jl package of the Julia programming language,[35] we minimized $\overline{C}(\mathcal{S})$ over the RF flip angles of $\mathcal{S}$. There were no explicit constraints on the flip angles, but to account for RF power constraints, we slightly modified the criterion by introducing a peak-power-correction factor, obtaining $C^{\text{overall}}(\mathcal{S}) = \overline{C}(\mathcal{S}) / \sqrt{1 + a\left(\frac{\pi - \text{Max}(\mathcal{S})}{\pi}\right)}$, where $\text{Max}(\mathcal{S})$ is the highest flip angle value of the sequence (in rad) and a has been chosen to be 0.57. In addition, we restricted the optimization to 20 equidistant values for the flip angle, and derived the remaining 1100 values by cubic-spline interpolation, similar to the approach presented by Mickevicius et al.[29] and particularly by

Scope Crafts et al.[36] To reduce the sensitivity to local minima, we applied a multilevel approach: first optimizing on 10 equidistant points, using the result as a basis for 15 points and the result thereof for a 20-point optimization. In each of these three steps, the number of Nelder–Mead iteration steps was limited to 2000.

The optimization process was followed by a selection process because the function $C^{\text{overall}}(\mathcal{S})$ has multiple local minima. By initiating the optimization with nine slightly different initial states, different local optima $\mathcal{S}_i^{\text{opt,2D}} = \underset{\mathcal{S}}{\text{argmin}}\left(C^{\text{overall}}(\mathcal{S})\right)$ were obtained, with $i = 1,...,9$. The superscript "2D" indicates that the optimization was performed in the context of phase encoding (see Figure 4C). The nine resulting shapes in Figure 4A seem mutually very different, indicating that not all of them can be the true optimum. Because we are dealing with a nonconvex minimization problem, the true optimum would require an exhaustive search, which would incur a prohibitive computational burden. But because the nine outcomes are mutually very close, this increases the confidence that all of them are close to the true optimum.

In a similar fashion, we also optimized on $\mathcal{S}$, assuming an absence of any encoding, resulting in sequences $\mathcal{S}_i^{\text{opt,0D}}$. Note that this 0D optimization approach is the most frequently adopted in the existing literature.[16–21,26,29]

To simplify the experimental validation, the best and the worst of each set was chosen based on the $C^{\text{overall}}(\mathcal{S})$ criterion. The flip angles of the resulting four sequences are called "2D-best", "2D-worst", "0D-best", and "0D-worst", where "best" and "worst" always refer to the performance in a 2D setting (i.e., including phase encoding) (Figure 4A,B).

3.3 | MR measurements

Our measurements were intended to validate and apply the BLAKJac framework. In particular, we investigated whether:

1. Experimentally obtained noise levels and spatial-frequency noise spectra correspond to those predicted by BLAKJac.
2. Sequences optimized taking into account the gradient-encoding scheme (2D-optimized) perform better than sequences optimized without it (0D-optimized).
3. Analytical tools (noise spectrum diagrams) derived from the BLAKJac framework successfully predict the spatial quantitative and qualitative behavior of a measured sequence. We performed MR-STAT measurements with the four sequences derived in subsection 3.2. To estimate standard deviations of the reconstructed parameter values, each scan was repeated 10 times (with a 7-s pause between subsequent scans). The measurements consisted of

- The "0D" measurements of a single vial (number 7) of the Eurospin phantom,[37] located in the isocenter, vial axis parallel to the main field direction, using a sagittal slice but with the phase-encoding gradient switched off. For each sequence type, the vial was scanned 10 times. Despite the name "0D", the frequency encoding was still active in the long axis of the vial; given the useful length of the liquid in the vial, 41 mm, we measured maps of the form $u_p(x;m)$, with $x = 1,...41$ and $m = 1,...,10$, and with $p \in \{T_1, T_2\}$. We calculated the standard deviations and the means over m and then we averaged these over x. Given that the estimate of a standard deviation from N_m measurements spreads as $\frac{\sigma}{\sqrt{2N_m - 2}}$, we obtained estimates of the standard deviations with a relative accuracy of $1/\sqrt{(2\times 10-2)\times 41}$, which is approximately 4%.
- A 2D axial slice of a phantom setup housing 16 vials of the Eurospin phantom.
- A 2D axial slice of the brain of two healthy volunteers (with approved consent according to the guidelines of the ethics committee).

The quantitative T_1 and T_2 maps for each experimental setup were obtained applying the MR-STAT reconstruction.[14,38,39]

4 | RESULTS

4.1 | Optimized sequences

The result of the sequence optimization is shown in Figure 4. As explained in section 3.2, two sets of RF sequences were obtained, called $\mathcal{S}_i^{\text{opt,2D}}$ and $\mathcal{S}_i^{\text{opt,0D}}$, with $i = 1,...,9$. We observe that these must be local optima because the evaluated performance within a set is not identical. Within the 2D-set $\mathcal{S}_i^{\text{opt,2D}}$, the ratio between the highest and lowest calculated noise level is 10%, that is, $\frac{\max_i\left(\mathcal{C}\left(\mathcal{S}_i^{\text{opt,2D}}\right)\right)}{\min_i\left(\mathcal{C}\left(\mathcal{S}_i^{\text{opt,2D}}\right)\right)} \approx 1.1$. Similarly, for the 0D-set $\mathcal{S}_i^{\text{opt,0D}}$, when evaluated on 0D, the noise level varies by 18% (highest to lowest ratio = 1.18). As opposed to this relatively small spread, when evaluated in the relevant 2D scenario, the ratio $\frac{\max_i\left(\mathcal{C}_{2D}\left(\mathcal{S}_i^{\text{opt,0D}}\right)\right)}{\min_i\left(\mathcal{C}_{2D}\left(\mathcal{S}_i^{\text{opt,0D}}\right)\right)}$ becomes 3.5, that is, 250% difference.

4.2 | Single-voxel ("0-D") measurements

The measured standard deviations for the 0-D phantom reconstructions are reported in Table 1.

Within the expected precision, the measured ratios between the sequence performances were in accordance with those predicted by BLAKJac: for a 0D-measurement (i.e., a measurement without phase encoding), the 0D-optimized results were marginally better than the 2D-optimized results. Table 1 also shows that the difference between 0D-best and 0D-worst is marginal. This is not surprising because these sequences were all optimized in a 0D-setting.

4.3 | Phantom 2D measurements

The 2D reconstruction results of the Eurospin phantom are shown in Figure 5. A high level of artefacts in the 0D-worst sequence is clearly visible. The standard deviations are displayed in Figure 6. The 0D-worst sequence resulted in noise levels that are approximately twice as high as those of the other sequences. This shows that there is a high performance spread among the 0D-optimized sequences, although they all performed almost equally well in a 0D setting. That spread is negligible among the 2D-optimized sequences.

From Figure 7, it is apparent that the 0D-optimized sequences, 0D-worst in particular, show substantially higher quantitative errors than the 2D-optimized sequences. These quantitative errors are attributed to poor rendition at the low spatial frequencies, as will be further elaborated in the Discussion section.

TABLE 1 Single-voxel ("0D") measurement (Measured) results

	T1 standard deviation (ms)		T2 standard deviation (ms)		
	Measured	BLAKJac	Measured	BLAKJac	Measured mean (T1, T2) (ms)
2D-best	4.6	4.18	0.83	0.52	(643, 61)
2D-worst	4.4	4.61	0.96	0.57	(646, 66)
0D-best	4.2	4.09	0.79	0.49	(639, 61)
0D-worst	4.0	4.35	0.79	0.53	(640, 61)

Note: the measured standard deviation is compared with the BLAKJac estimate (the scaling factor was chosen to maximally match the measured T1 results). The obtained mean (T1, T2) values are reported in the last column. The main message is that the 0D-optimized sequences perform slightly better when applied on 0D than 2D-optimized sequences do when applied on 0D. This can be seen by the deviations in the last two rows being slightly lower compared with the "2D" rows.
Abbreviation: BLAKJac, BLock Analysis of a K-space-domain Jacobian.

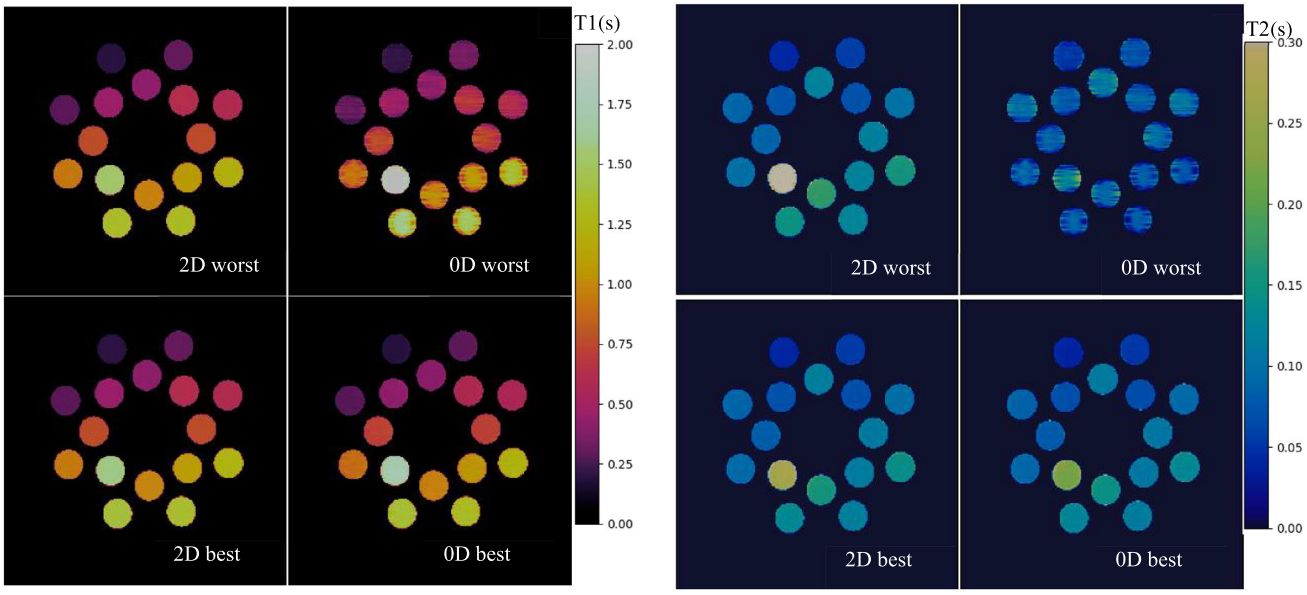

FIGURE 5 Reconstructed maps (left T1, right T2) of the phantom setup with the Eurospin vials. It can be seen that the 2D-optimized results have consistent image quality, while the 0D-optimized results do not – although the 0D-optimized sequences score mutually very similarly in a 0D-setting

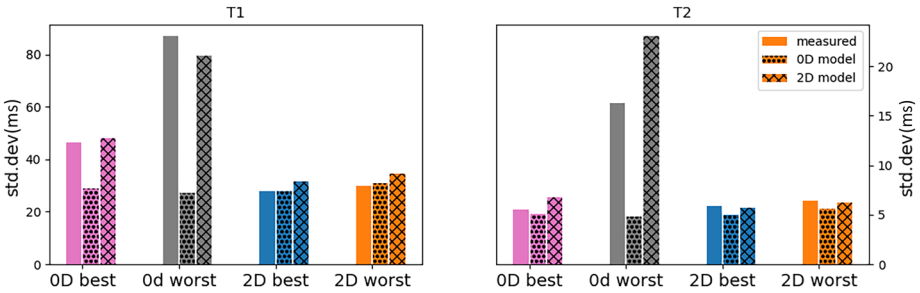

FIGURE 6 Measured standard deviations (nonpatterned bars), averaged over all vials. The patterned bars represent the BLAKJac predictions of the standard deviations for a seven-tissue mix (see section 3.2). The cross-hatched bars represent the predictions in the "2D" approach, that is, analyzed in the context of phase encoding, while the bulleted bars represent predictions according to the single-voxel ("0D") optimization approach. It can be seen that the 0D-approach (bulleted bars) predicts very similar noise performance for all sequences (even indicating that "0D worst" would be slightly better than the others); to the contrary, a 2D-analysis in BLAKJac (cross-hatched) is able to indicate that some sequences perform significantly worse in the actual scenario (i.e., with spatial encoding). These predictions match substantially better with the measured noise levels (solid bars). Consequently, the 2D-optimized sequences display consistent noise level, while the 0D-optimized sequences do not. BLAKJac, BLock Analysis of a K-space-domain Jacobian

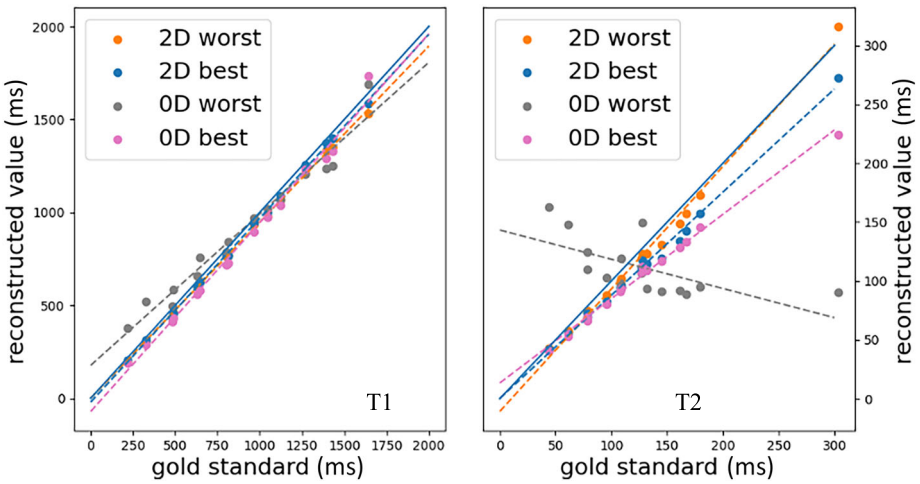

FIGURE 7 Correspondence between reconstructed mean values and gold standard for the Eurospin vials (bullets). Each bullet represents a gel-filled vial. The dashed lines are the linear regression lines through the bullets. The full blue diagonal is the identity line. The 0D-worst optimization is clearly inferior, particularly on T2, where the relation to the gold standard value is lost or even slightly inverted. Also here, the message is that the 2D-optimized results are mutually consistent, while the 0D-optimized results are not

4.4 | In vivo 2D measurements

In vivo results for the four types of scan are shown in Figure 8. It is clear that the 0D-worst results are inferior to the others in several aspects. This is also reflected in the measured standard deviations (Figure 9). In addition, the 0D-sequences clearly create biased maps (with substantial differences between "best" and "worst"). This is compatible with Figure 8 (phantom bias) for $T_1 \approx 1000$ and $T_2 \approx 70$. Section 5 (Discussion) elaborates on a likely reason for the 0D-sequences to show more bias.

Each scan was repeated 10 times, providing a pixel-wise estimate of the standard deviation with a relative precision of $1/\sqrt{2 \times N_{\text{repetitions}} - 2} \approx 0.24$. To further increase the accuracy of the estimate, we averaged the standard deviation (a) over an ROI of 20 x 20 pixels of presumed pure white matter, and (b) over the whole image.

4.5 | Noise spectra analysis

As explained in section 2.3.1, BLAKJac can predict the spatial spectra of the resulting noise. The predicted spectra for all nine sequences are plotted in Figure 10. These have been obtained as an average over seven different combinations of $\left(T_1^{\text{ref}}, T_2^{\text{ref}}\right)$, but the outcome does not strongly

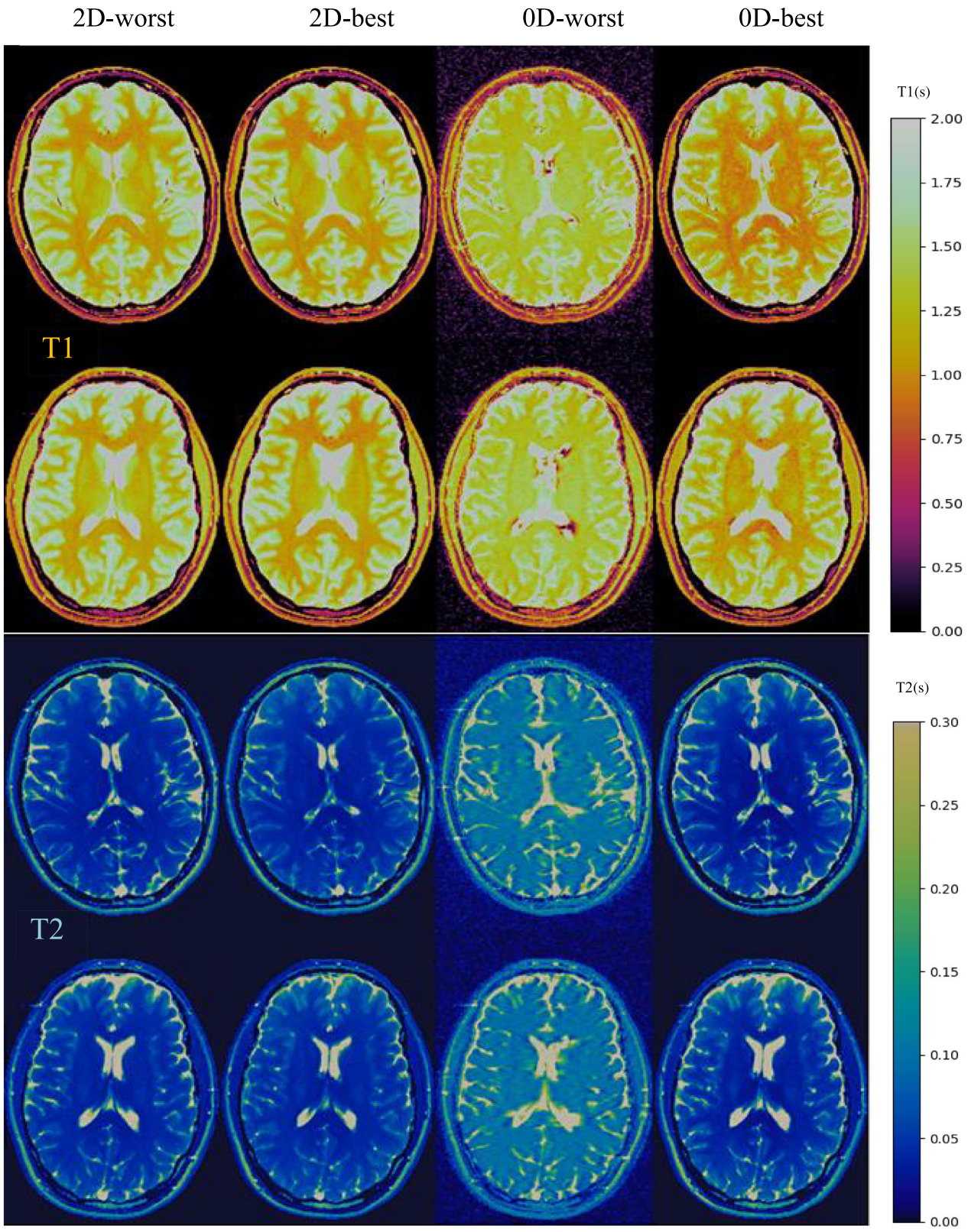

FIGURE 8 Reconstructed maps of two volunteers (one in rows 1 and 3, the other in rows 2 and 4). The columns represent the four applied sequences. The color bars express the relaxation time in seconds. While the 2D-results are mutually similar, the 0D-results are not

depend on the selected $\left(T_1^{\text{ref}}, T_2^{\text{ref}}\right)$. The resulting figure shows a much higher consistency among the nine spectra of the 2D-optimized sequences than among the 0D-optimized. Most notably, the 0D-optimized sequences tend to have peaks on unexpected spectral locations; some of them, particularly the one denoted as "worst" (in gray), happen to have their peak at the low spatial frequencies ($|k_y| \approx 0$).

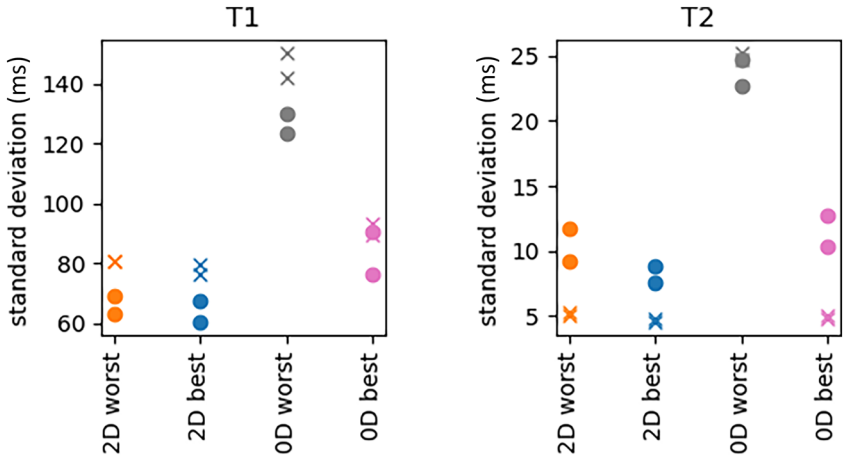

FIGURE 9 Standard deviations in the maps of the two volunteers, averaged over a region of interest in the white matter (crosses) and averaged over the whole image (bullets)

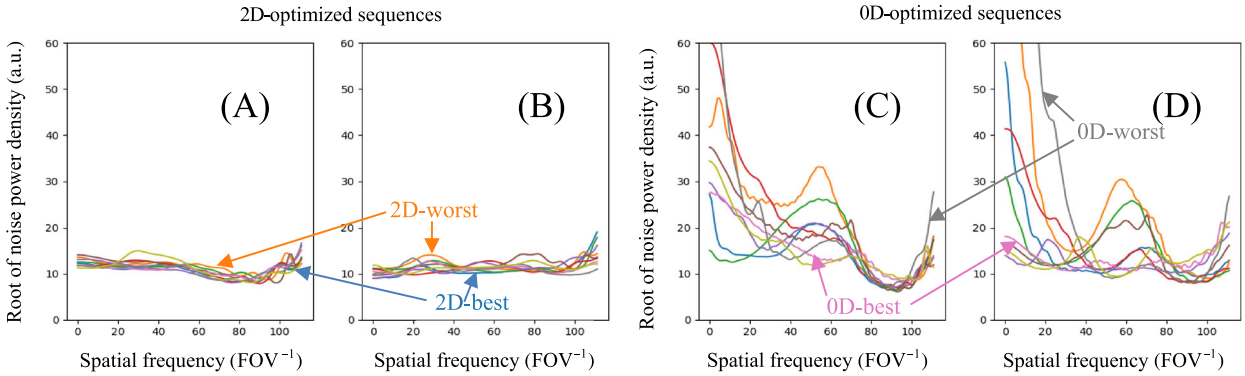

FIGURE 10 BLAKJac-calculated spectra for (A and C) T1 and (B and D) T2 of nine realizations of 2D-optimized sequences (A and B) and of nine realizations of single-voxel–optimized sequences (C and D). The sequences are shown in Figure 4. The dispersion of the curves in (C) and (D) shows that a single-voxel–optimized sequence has an unpredictable outcome when applied in a setup with phase encoding, while the outcome is much more predictable when applying 2D-optimization (A and B). Evaluation was performed assuming a seven-tissues mix (see section 3.2). BLAKJac, BLock Analysis of a K-space-domain Jacobian

Data from the phantom and the volunteers allow to estimate noise spectra and thus validate the BLAKJac predictions. Because we have 10 realizations of T_1- and T_2-maps for each sequence, we can Fourier-transform these maps in both dimensions then take the standard deviations over the realizations.

Figure 11 shows the BLAKJac-generated spectra (dashed lines) alongside the measured spectra for the phantom. Most spectral features from the BLAKJac prediction are clearly recognizable in the measured noise spectra.

5 | DISCUSSION

We present a methodology, called BLAKJac, which can evaluate the precision performance of the combined time-varying RF train and gradient-encoding scheme in only a few milliseconds, allowing for flip-angle optimizations in the context of spatial encoding.

To show the added value of the BLAKJac analysis, we compared RF-flip-angle sequences that, on one hand, have been single-voxel–optimized (i.e., ignoring the spatial encoding, or "0D"), and, on the other hand, sequences that have been optimized in the context of phase encoding ("2D"). We have shown that a set of 0D-optimized sequences, which all lead to mutually very similar noise levels when analyzed in a 0D-setting, do lead to very unpredictable performance in the relevant scenario, that is, when spatial encoding is active (2D). On the other hand, the set of 2D-optimized sequences based on the BLAKJac criterion are mutually of very similar performance and, in general, outperform the 0D-optimized sequences. This is shown in phantoms as well as in vivo measurements (Figures 6 and 9, respectively); the actually achieved noise level

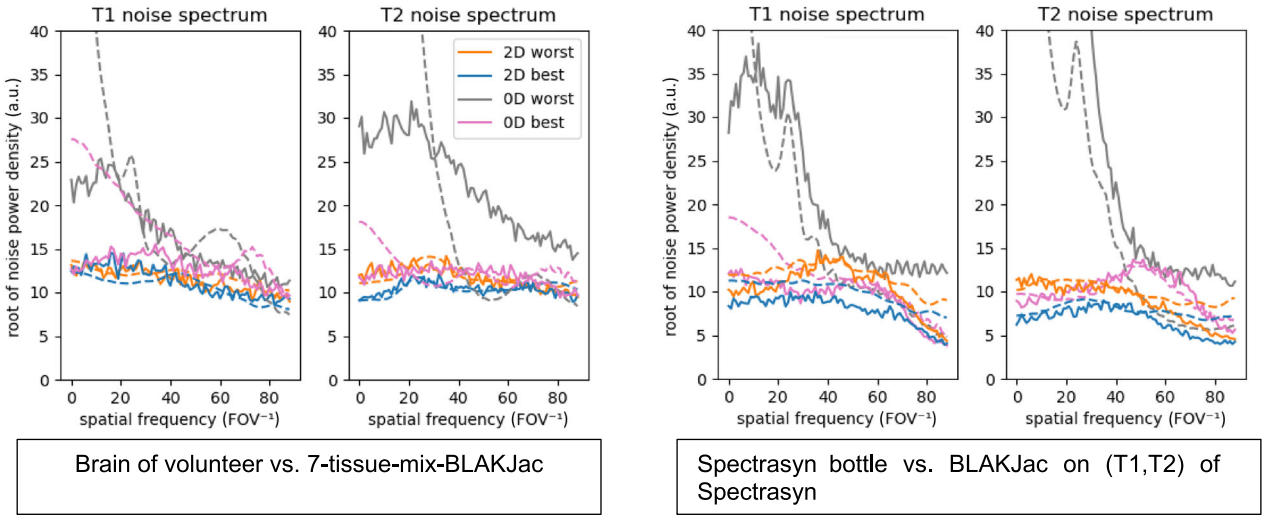

FIGURE 11 Measured spectra (full lines) and the corresponding BLAKJac-predicted spectra (dashed lines). Left: in the brain of a volunteer (section 4.4); right: in a measurement of a 5-L bottle filled with mineral oil (Spectrasyn). For the brain, the BLAKJac predictions are based on a mix of seven human tissues (see 3.2); for the mineral-oil phantom, the (T1, T2) values of that liquid were assumed [(T1, T2) = (300 ms, 100 ms)]. BLAKJac, BLock Analysis of a K-space-domain Jacobian

of the 0D-optimized sequences can be substantially higher than the noise level in 2D-optimized sequences. These findings are a natural consequence of the BLAKJac analysis: if the time-varying flip angle is evaluated in conjunction with the underlying gradient-encoding scheme (2D-optimization), the spatial noise spectra exhibit a much higher level of control (Figure 10A,B). The performance of 0D-optimized sequences strongly depends on the initialization condition of the optimization process: sequences that are almost equally optimal in the single-voxel sense (e.g., the 0D-best and 0D-worst sequence) lead to widely varying outcomes in actual phase-encoded measurements.

Another feature of BLAKJac is its ability to calculate expected noise levels and spatial noise spectra in tissue-parameter maps. We show that spatial noise spectra reconstructed from measurements match the BLAKJac-predicted spectra (Figure 11). The noise spectra analysis is helpful to gain insights into the 0D optimization process: the 0D-optimized sequences display a characteristically peaked noise spectrum (Figure 10C,D). This can be particularly unfavorable if a peak emerges in the low spatial frequencies (around $|k_y| = 0$, or around $|\boldsymbol{k}| = 0$): these spatial frequencies are not only affected by noise, but model errors—which will be discussed extensively below—also predominantly affect the low spatial frequencies. As a consequence, model errors are multiplied by the BLAKJac-calculated factor $\left(\boldsymbol{J}^H_{\Gamma/\mathrm{f}}\boldsymbol{J}_{\Gamma/\mathrm{f}}\right)^{-1}$ at low spatial frequencies; this factor happens to be particularly high for the 0D-worst sequence (as in the gray curves of Figure 10C,D). This, in turn, causes a significant error in reconstructed T_1 and T_2 values in 0D-optimized sequences. In contrast to 0D-optimized sequences, the spectra of 2D-optimized sequences do not display peaks.

While Figures 6 and 9 show that the noise standard deviation is highest with the 0D-worst sequence, Figures 5, 7, and 8 also show substantially increased quantitative errors for, in particular, the 0D-worst sequence. This is most clearly seen in the dashed gray line in the right half of Figure 7, indicating that the reconstructed T_2 of that sequence has a negative correlation with the true T_2.

In essence, our approach focuses on precision. As in all inversion problems, accuracy will be affected by differences (i.e., "model errors") between the true underlying physics and the applied model. These model errors can have various causes, including erroneous knowledge of the B_1^+ field, erroneous slice profile, erroneously assuming a single-species model in each voxel,[40] neglecting magnetization transfer,[41] and neglecting diffusion weighting induced by the sequence,[42] etc. We do have some indications that the accuracy, for example, the extent to which diffusion influences the T_2 estimate, does depend on the sequence. This might explain the difference in bias in T_2 between the 2D-worst, 2D-best, and 0D-best sequences, which, according to BLAKJac, result in very similar performance (i.e., very similar performance in terms of precision).

Although it is beyond the scope of this paper, it is certainly indicated to study the relation between sequence and accuracy (e.g., T_2- dependence on B_1^+ or diffusion), and to subsequently minimize these dependences. These dependences are a factor in the inaccuracy (or bias). In addition to these dependences, there is another factor influencing the bias that can be directly tackled by BLAKJac, namely, the value of $\left(\left(\boldsymbol{J}^H_{\Gamma/\mathrm{f}}\boldsymbol{J}_{\Gamma/\mathrm{f}}\right)^{-1}\right)_{(\boldsymbol{k},\,\boldsymbol{p}),(\boldsymbol{k},\,p)}$ for low spatial frequencies ($|\boldsymbol{k}| \sim \boldsymbol{0}$). As can be seen from the gray curves of Figure 10C,D, this value is particularly high for the 0D-worst sequence. Empirically, for the 2D-optimization, we found it beneficial to penalize the matrices $\left(\left(\boldsymbol{J}^H_{\Gamma/\mathrm{f}}\boldsymbol{J}_{\Gamma/\mathrm{f}}\right)^{-1}\right)_{(\boldsymbol{k},\,\boldsymbol{p}),(\boldsymbol{k},\,p)}$ with a weighting factor of 3.0 for $\boldsymbol{k} = 0$, gradually decaying to 1.0 at $|\boldsymbol{k}| = 20$. This operation is irrelevant for the 0D-optimization: in the absence of encoding, each sample is considered to be at $\boldsymbol{k} = 0$.

Particularly when optimizing a multiplicity of parameters—in our case, 20—optimization might lead to false minima. The nine resulting shapes in Figure 4A seem mutually very different, indicating that not all of them can be the true optimum. Because we are dealing with a nonconvex minimization problem, the true optimum would require an exhaustive search, which would incur a prohibitive computational burden. But because the nine outcomes are mutually very close, this increases the confidence that all of them are close to the true optimum. Likewise, the optimization outcomes of the 0D-sequences in Figure 4B are also mutually very similar—if evaluated in a 0D-context—but they differ substantially when evaluated in a 2D-context. That variation is not caused by finding false optima, but is the result of optimizing in a 0D context and applying them to the relevant scenario (i.e., 2D).

In principle, the BLAKJac methodology applies equally to non-Cartesian sequences, like those frequently used in MRF, which typically adopt spiral or radial encoding strategies. Yet, BLAKJac does not necessarily apply to any type of MRF reconstruction. The basic MRF reconstruction approach via a dictionary match of strongly undersampled images[13] is characterized by an additional perturbation term, which consists of aliasing artefacts. These kind of perturbations are not captured by BLAKJac, which studies the CRLB, as derived from purely stochastic (thermal) noise. We hypothesize that BLAKJac should be applicable to MRF sequences reconstructed using advanced inverse problem techniques,[43,44] which better approach the ideal result expressed by the CRLB.

Although the BLAKJac methodology is applicable to a broad category of encoding patterns, in this work we focused on a Cartesian approach using MR-STAT. We chose to not take coil sensitivity into account, and thus we do not elaborate on parallel imaging. Intuitively, if the RF-flip-angle patterns are smooth with respect to the phase-encoding index (as in our MR-STAT examples), one can regard undersampling-pattern optimizations[27] as being independent of the optimizations of the flip-angle pattern and therefore they can be treated separately. Parallel imaging with generalized encoding schemes (e.g., spiral and golden angle radial) can be included in principle, although the resulting formalism would substantially increase in complexity, and this would go beyond the scope of this paper.

Further potential applications of BLAKJac include sequences of RF flip angles with optimized phase variation, optimization of 3D sequences, and potential extension to other parameters such as B1+. Constraints such as maximum specific absorption rate can be easily incorporated into BLAKJac. Also, BLAKJac may be applied to optimize the encoding pattern given a flip angle sequence, or to optimize encoding and flip angle jointly. Finally, the clinical application of BLAKJac-optimized sequences will be the subject of future research.

6 | CONCLUSION

The proposed BLAKJac analysis is an efficient methodology for evaluating the precision performance of transient-state multiparametric MRI sequences (like MR-STAT) in the context of applied gradient encoding. The noise levels and spectra predicted by BLAKJac correspond to those measured in vivo and in phantoms. Because the calculations take only few milliseconds, BLAKJac can optimize sequences taking into account the phase encoding. This is shown to have clear benefits in MR-STAT over single-voxel optimization. BLAKJac, which uses the 2D-encoding information, is much better at predicting the actual noise level in images compared with a single-voxel approach.

ACKNOWLEDGMENTS

This work has been financed by Nederlandse Organisatie voor Wetenschappelijk Onderzoek (NWO) grant number 17986, which has partly been funded by the company Philips.

ORCID

Miha Fuderer https://orcid.org/0000-0002-5673-915X

REFERENCES

1. Pykett IL, Mansfield P. A line scan image study of a tumorous rat leg by NMR. *Phys Med Biol*. 1978;23:961-967. doi:10.1088/0031-9155/23/5/012
2. Edelstein WA, Hutchison JMS, Johnson G, Redpath T. Spin warp NMR imaging and applications to human whole-body imaging. *Phys Med Biol*. 1980; 25(4):751-756. doi:10.1088/0031-9155/25/4/017
3. Kaufman L, Crooks LE, Margulis AR. *Nuclear Magnetic Resonance Imaging in Medicine*. Igaku-Shoin Medical Publishers; 1981.
4. Shcherbakova Y, van den Berg CAT, Moonen CTW, Bartels LW. PLANET: An ellipse fitting approach for simultaneous T_1 and T_2 mapping using phase-cycled balanced steady-state free precession. *Magn Reson Med*. 2018;79(2):711-722. doi:10.1002/mrm.26717
5. Chen Y, Liu S, Wang Y, Kang Y, Haacke EM. STrategically Acquired Gradient Echo (STAGE) imaging, part I: Creating enhanced T1 contrast and standardized susceptibility weighted imaging and quantitative susceptibility mapping. *Magn Reson Imaging*. 2018;46:130-139. doi:10.1016/j.mri.2017.10.005
6. Wang X, Tan Z, Scholand N, Roeloffs V, Uecker M. Physics-based reconstruction methods for magnetic resonance imaging. *Phil Trans Royal Soc A Math Phys Eng Sci*. 2021;379(2200):20200196. doi:10.1098/rsta.2020.0196
7. Ma S, Wang N, Fan Z, et al. Three-dimensional whole-brain simultaneous T1, T2, and T1 ρ quantification using MR multitasking: Method and initial clinical experience in tissue characterization of multiple sclerosis. *Magn Reson Med*. 2021;85(4):1938-1952. doi:10.1002/mrm.28553

8. Marquet C, Jang J, Powell A, Moghari MH. Rapid simultaneous T1 and T2 quantification (RAS-Q T1T2) of the myocardium using transient bSSFP with variable flip angles. In: *Abstracts of the ISMRM*; 2021:0901.
9. Velasco C, Cruz G, Botnar RM, Prieto C. Simultaneous comprehensive T1, T2, T2*, T1P and Fat Fraction characterization with Magnetic Resonance Fingerprinting. In: *Abstracts of the ISMRM*; 2021:0171.
10. Roeloffs V, Scholand N, Uecker M. Fast-Sweep Frequency-Modulated SSFP: Boosting Sensitivity for 3D Joint T1/T2 Mapping. In: *Abstracts of the ISMRM*; 2021:3052.
11. Kotek G, Nunez-Gonzalez L, Vogel MW, Krestin GP, Poot DHJ, Hernandez-Tamames JA. From signal-based to comprehensive magnetic resonance imaging. *Sci Rep*. 2021;11(1):1-13.
12. Assländer J. A perspective on MR fingerprinting. *J Magn Reson Imaging*. 2021;53(3):676-685.
13. Ma D, Gulani V, Seiberlich N, et al. Magnetic resonance fingerprinting. *Nature*. 2013;495(7440):187-192.
14. van der Heide O, Sbrizzi A, Luijten PR, van den Berg CAT. High-resolution in vivo MR-STAT using a matrix-free and parallelized reconstruction algorithm. *NMR Biomed*. 2020;33(4):e4251.
15. Sbrizzi A, van der Heide O, Cloos M, et al. Fast quantitative MRI as a nonlinear tomography problem. *Magn Reson Imaging*. 2018;46:56-63.
16. Assländer J, Lattanzi R, Sodickson DK, Cloos MA. Optimized quantification of spin relaxation times in the hybrid state. *Magn Reson Med*. 2019;82(4):1385-1397.
17. Zhao B, Haldar JP, Setsompop K, Wald LL. Optimal experiment design for magnetic resonance fingerprinting. In: *2016 38th Annual International Conference of the IEEE Engineering in Medicine and Biology Society (EMBC)*; 2016:453-456.
18. Cohen O, Rosen MS. Algorithm comparison for schedule optimization in MR fingerprinting. *Magn Reson Imaging*. 2017;41:15-21.
19. Sommer K, Amthor T, Doneva M, Koken P, Meineke J, Börnert P. Towards predicting the encoding capability of MR fingerprinting sequences. *Magn Reson Imaging*. 2017;41:7-14.
20. Heesterbeek D, Vos F, van Gijzen M, Nagtegaal M. Sequence Optimisation for Multi-Component Analysis in Magnetic Resonance Fingerprinting. In: *Abstracts of the ISMRM*; 2021:1561.
21. Zhao B, Haldar JP, Liao C, et al. Optimal experiment design for magnetic resonance fingerprinting: Cramér-Rao bound meets spin dynamics. *IEEE Trans Med Imaging*. 2018;38(3):844-861.
22. Loktyushin A, Herz K, Dang N, et al. MRzero-Automated discovery of MRI sequences using supervised learning. *Magn Reson Med*. 2021;86(2):709-724.
23. Körzdörfer G, Pfeuffer J, Kluge T, et al. Effect of spiral undersampling patterns on FISP MRF parameter maps. *Magn Reson Imaging*. 2019;62:174-180.
24. Kara D, Fan M, Hamilton J, Griswold M, Seiberlich N, Brown R. Parameter map error due to normal noise and aliasing artifacts in MR fingerprinting. *Magn Reson Med*. 2019;81(5):3108-3123.
25. Stolk CC, Sbrizzi A. Understanding the combined effect of {k} - space undersampling and transient states excitation in MR fingerprinting reconstructions. *IEEE Trans Med Imaging*. 2019;38(10):2445-2455.
26. Lee PK, Watkins LE, Anderson TI, Buonincontri G, Hargreaves BA. Flexible and efficient optimization of quantitative sequences using automatic differentiation of Bloch simulations. *Magn Reson Med*. 2019;82(4):1438-1451.
27. Byanju R, Klein S, Cristobal-Huerta A, Hernandez-Tamames JA, Poot DHJ. Time efficiency analysis for undersampled quantitative MRI acquisitions. *Med Image Anal*. 2022;78:102390.
28. Leitão D, Teixeira RPAG, Price A, Uus A, Hajnal JV, Malik SJ. Efficiency analysis for quantitative MRI of T1 and T2 relaxometry methods. *Phys Med Biol*. 2021;66(15):15NT02..
29. Mickevicius NJ, Nencka AS, Paulson ES. Reducing the Dimensionality of Optimal Experiment Design for Magnetic Resonance Fingerprinting. *arXiv*:201000674;2020.
30. Jordan SP, Hu S, Rozada I, et al. Automated design of pulse sequences for magnetic resonance fingerprinting using physics-inspired optimization. *Proc Natl Acad Sci*. 2021;118(40):e2020516118..
31. Sbrizzi A, Bruijnen T, van der Heide O, Luijten P, van den Berg CAT. Dictionary-free MR Fingerprinting reconstruction of balanced-GRE sequences. *arXiv*:171108905;2017.
32. Assländer J, Novikov DS, Lattanzi R, Sodickson DK, Cloos MA. Hybrid-state free precession in nuclear magnetic resonance. *Commun Phys*. 2019;2(1):1-12.
33. Weigel M. Extended phase graphs: dephasing, RF pulses, and echoes-pure and simple. *J Magn Reson Imaging*. 2015;41(2):266-295.
34. White JM, Holy T, Mogensen PK, Riseth AN. Optim.jl. https://julianlsolvers.github.io/Optim.jl/stable/#algo/nelder_mead/
35. Bezanson J, Edelman A, Karpinski S, Shah VB. Julia: A fresh approach to numerical computing. *SIAM Rev*. 2017;59(1):65-98.
36. Scope Crafts E, Lu H, Ye H, Wald LL, Zhao B. An efficient approach to optimal experimental design for magnetic resonance fingerprinting with B-splines. *Magn Reson Med*. 2022;88(1):239-253.
37. Diagnostic Sonar Ltd. Eurospin II magnetic resonance quality assessment test object 5; 1995.
38. van der Heide O, Sbrizzi A, van den Berg CAT. Faster Bloch simulations and MR-STAT reconstructions on GPU using the Julia programming language. In: *Abstracts of the ISMRM*; 2021:3063.
39. Liu H, van der Heide O, van den Berg CAT, Sbrizzi A. Fast and accurate modeling of transient-state, gradient-spoiled sequences by recurrent neural networks. *NMR Biomed*. 2021;34(7):e4527.
40. Reynolds LA, Morris SR, Vavasour IM, Barlow L, MacKay AL, Michal CA. Proceedings of the ISMRM. In: *T1 Relaxation of White Matter Following Adiabatic Inversion*; 2021:3074.
41. Teixeira RPAG, Malik SJ, Hajnal JV. Fast quantitative MRI using controlled saturation magnetization transfer. *Magn Reson Med*. 2019;81(2):907-920. doi:10.1002/mrm.27442
42. Kobayashi Y, Terada Y. Diffusion-weighting caused by spoiler gradients in the fast imaging with steady-state precession sequence may lead to inaccurate T 2 measurements in MR fingerprinting. *Magn Reson Med Sci*. 2019;18(1):96-104. doi:10.2463/mrms.tn.2018-0027
43. Zhao B, Setsompop K, Ye H, Cauley SF, Wald LL. Maximum likelihood reconstruction for magnetic resonance fingerprinting. *IEEE Trans Med Imaging*. 2016;35(8):1812-1823.
44. Assländer J, Cloos MA, Knoll F, Sodickson DK, Hennig J, Lattanzi R. Low rank alternating direction method of multipliers reconstruction for MR fingerprinting. *Magn Reson Med*. 2018;79(1):83-96. doi:10.1002/mrm.26639

45. Wright PJ, Mougin OE, Totman JJ, et al. Water proton T 1 measurements in brain tissue at 7, 3, and 1.5 T using IR-EPI, IR-TSE, and MPRAGE: results and optimization. *Magn Reson Mater Phys Biol Med*. 2008;21(1):121-130.

How to cite this article: Fuderer M, van der Heide O, Liu H, van den Berg CAT, Sbrizzi A. Efficient performance analysis and optimization of transient-state sequences for multiparametric magnetic resonance imaging. *NMR in Biomedicine*. 2023;36(3):e4864. doi:10.1002/nbm.4864

APPENDIX A

A.1 | TAYLOR EXPANSION OF THE MODEL Γ AND FACTORIZATION OF THE JACOBIAN

A.1.1 | Taylor expansion of the signal model Γ

Consider the signal function Γ at the time points at which the data samples, denoted as $d_{\boldsymbol{k},i}$, are acquired. The corresponding data model is written as $\Gamma_{\boldsymbol{k},i}$. A data sample is characterized by the encoding $\boldsymbol{k}$ – but not fully characterized by it, because several samples (possibly distant in time) may be acquired with the same encoding. The additional index i (denoted as "instance" in the sequel) can be read as "the i-th time that a datapoint has been taken at k-space coordinate $\boldsymbol{k}$" (see the orange line in Figure 4C). We assume the number of instances to be equal for all sampled coordinates $\boldsymbol{k}$, so that $i = 1,\ldots,N_{\text{instances}}$ for each $\boldsymbol{k}$.

We model $\Gamma_{\boldsymbol{k},i}$ as a sum of contributions from discrete voxels:

$$\Gamma_{\boldsymbol{k},i} = \sum\nolimits_{\boldsymbol{r}} u_{0,\boldsymbol{r}} G_{(\boldsymbol{k},\, i)}\left(u_{1,\boldsymbol{r}},\, \ldots,\, u_{(N_p-1),\boldsymbol{r}}\right) e^{i2\pi \boldsymbol{k}\cdot\boldsymbol{r}}. \tag{A1}$$

The proton-density ($\boldsymbol{u}_0$) is treated differently from all other properties $\boldsymbol{u}_{p\geq 1}$ (e.g., T_1, T_2), because the proton-density enters the MR signal model as a purely linear factor. The function $G_{(\boldsymbol{k},\, i)}$ denotes the "net transverse magnetization". If multiplied by the proton density, $G_{(\boldsymbol{k},\, i)}$ gives the local signal contribution. Note that G is closely related to Γ, but the latter also contains the spatial encoding, while the function G does not. Therefore, G could be described as the Bloch model at timepoint $(\boldsymbol{k}, i)$ given the relaxation properties $u_{1,\boldsymbol{r}},\ldots,u_{(N_p-1),\boldsymbol{r}}$ at any location $\boldsymbol{r}$.

Note that, for simplicity of the discourse, the coil sensitivity has been left out of the model: a single—and perfectly uniform—coil element is assumed here.

We assume that, for the purpose of a Cramér–Rao analysis, the function $G_{(\boldsymbol{k},\, i)}\left(u_{1,\boldsymbol{r}},\, \ldots,\, u_{(N_p-1),\boldsymbol{r}}\right)$ can be accurately described by its first-order Taylor component, because Appendix B shows that the second-order components are expected to be negligible. Using that assumption, we can write

$$G_{(\boldsymbol{k},\, i)}\left(u_{1,\boldsymbol{r}},\, \ldots,\, u_{(N_p-1),\boldsymbol{r}}\right) \approx g_{(\boldsymbol{k},\, i)} + \sum_{p=1}^{N_p-1}\left[\frac{\partial G_{(\boldsymbol{k},\, i)}}{\partial u_p}\Big|_{\boldsymbol{u}=\boldsymbol{u}^{\text{ref}}} \cdot \left(u_{p,\boldsymbol{r}} - u_p^{\text{ref}}\right)\right]. \tag{A2}$$

For example, $\frac{\partial G_{(\boldsymbol{k},\, i)}}{\partial u_1}\Big|_{\boldsymbol{u}=\boldsymbol{u}^{\text{ref}}}$ can be seen as "the level of T1-weighting" at time point $(\boldsymbol{k}, i)$. The values, u_p^{ref}, with $p = 1,\ldots,N_p - 1$, are arbitrary reference values that are chosen to be constant over the whole volume. For the validity of the subsequent approximations, u_p^{ref} is set as the middle point of the expected parameter's range. For instance, for T_1 in brain imaging, we may choose $u_1^{\text{ref}} \equiv T_1^{\text{ref}} = 900\,\text{ms}$, which is approximately the mean value of the combined gray/white matter at 1.5 T.[45] In Equation (A2), the symbol $g_{(\boldsymbol{k},\, i)}$ refers to the value of $G_{(\boldsymbol{k},\, i)}$ for the reference values u_p^{ref}. In addition, the shorthand $w_{p,\boldsymbol{k},i}$ will be introduced as

$$\begin{aligned} w_{p\geq 1,\boldsymbol{k},i} &= u_p^{\text{ref}} \cdot \frac{\partial G_{(\boldsymbol{k},\, i)}}{\partial u_p}\Big|_{\boldsymbol{u}=\boldsymbol{u}^{\text{ref}}} \\ w_{0,\boldsymbol{k},i} &= g_{(\boldsymbol{k},\, i)} \end{aligned}. \tag{A3}$$

With these notations, the relation between the unknowns $\boldsymbol{u}$ and the modeled response Γ can be approximated as

$$\Gamma_{\boldsymbol{k},i} \approx \sum\nolimits_{\boldsymbol{r}} \left\{ u_{0,\boldsymbol{r}} g_{\boldsymbol{k},i} + \sum_{p=1}^{N_p-1}\left[w_{p,\boldsymbol{k},i} \cdot u_{0,\boldsymbol{r}} \left(\frac{u_{p,\boldsymbol{r}}}{u_p^{\text{ref}}} - 1\right)\right]\right\} e^{i2\pi \boldsymbol{k}\cdot\boldsymbol{r}}, \tag{A4}$$

which can be written as

$$\Gamma_{\boldsymbol{k},i} \approx g_{\boldsymbol{k},i} \sum\nolimits_{\boldsymbol{r}} u_{0,\boldsymbol{r}} e^{2\pi j \boldsymbol{k}\cdot\boldsymbol{r}} + \sum_{p=1}^{N_p-1} \left[w_{p,\boldsymbol{k},i} \cdot \sum_{\boldsymbol{r}} u_{0,\boldsymbol{r}} \left(\frac{u_{p,\boldsymbol{r}}}{u_p^{\text{ref}}} - 1 \right) e^{i2\pi \boldsymbol{k}\cdot\boldsymbol{r}} \right]. \tag{A5}$$

A.1.1 | Factorization of the Jacobian

Using the definition of the auxiliary variables defined in Equation (2), we can write

$$\Gamma_{\boldsymbol{k},i} \approx w_{0,\boldsymbol{k},i} f_{0,\boldsymbol{k}} + \sum_{p=1}^{N_p-1} w_{p,\boldsymbol{k},i} \cdot f_{p,\boldsymbol{k}} = \sum_{p=0}^{N_p-1} w_{p,\boldsymbol{k},i} \cdot f_{p,\boldsymbol{k}}. \tag{A6}$$

From Equation (A6), it is clear that $\frac{\partial \Gamma_{\boldsymbol{k},i}}{\partial f_{p,\boldsymbol{l}}} \approx 0$ if $\boldsymbol{k} \neq \boldsymbol{l}$; this tells that, if a system is linear, a sample with spatial encoding $\boldsymbol{k}$ will not be sensitive to a different spatial frequency $\boldsymbol{l}$ of the maps $\boldsymbol{u}_0 \odot \left(\frac{\boldsymbol{u}_p}{\boldsymbol{u}_p^{\text{ref}}} - \boldsymbol{1} \right)$. Consequently, from Equation (A6), it follows that the Jacobian matrix $\boldsymbol{J}_{\Gamma/\text{f}} = \left[\frac{\partial \Gamma_{\boldsymbol{k},i}}{\partial f_{p,\boldsymbol{l}}} \right]$ has N_k nonzero blocks of size $N_{\text{instances}} \times N_p$ and content $w_{p,\boldsymbol{k},i}$ (where $\boldsymbol{k} = \boldsymbol{l}$), and that all the other blocks (i.e., where $\boldsymbol{k} \neq \boldsymbol{l}$) are zero. The matrix $\boldsymbol{J}_{\Gamma/\text{f}}$ is thus block-diagonal, or $j_{(\boldsymbol{k},\,i),(p,\,\boldsymbol{l})} \approx w_{p,\boldsymbol{k},i}\, \delta_{\boldsymbol{k},\boldsymbol{l}}$, with δ being a Kronecker operator. In other words, the elements of $\boldsymbol{J}_{\Gamma/\text{f}}$ are substantially nonzero only if the block-index of a row (i.e., pertaining to the encoding value of an element of $\boldsymbol{\Gamma}$) equals the block-index of the column (i.e., pertaining to the spatial-frequency element of $\boldsymbol{f}$).

We point out that there is an exception to the above conclusion if the properties $u_{p,\boldsymbol{r}}$ can be considered to be real-valued, as it is the case for the relaxation parameters T_1 and T_2: in this case, dependence emerges between $f_{p,\boldsymbol{k}}$ and $f_{p,-\boldsymbol{k}}$, leading to a matrix that has both a diagonal and an antidiagonal component. This is further elaborated in Appendix C.

APPENDIX B

B.1 | HIGHER-ORDER TERMS

In the hypothetical case where the signal model would be sufficiently described by a first-order Taylor expansion of the function G around $\boldsymbol{u}^{\text{ref}}$, it has been shown that the off-diagonal elements of $\boldsymbol{J}_{\Gamma/\text{f}}$ are zero. This Appendix elaborates on these off-diagonal elements in the situation that G also has substantial second-order Taylor components.

For the sake of brevity, we simplify the situation, assuming that we have just one unknown property $u_{1,\boldsymbol{r}}$ next to the proton density $u_{0,\boldsymbol{r}}$. Any additional second-order Taylor terms would follow an equivalent analysis, as well as Taylor terms associated with cross-products, for example, $\frac{\partial^2 G_{\text{time}(\boldsymbol{k},\,i)}}{\partial u_1 \partial u_2}\big|_{\boldsymbol{u}=\boldsymbol{u}^{\text{ref}}} \cdot \left(u_{1,\boldsymbol{r}} - u_1^{\text{ref}}\right)\left(u_{2,\boldsymbol{r}} - u_2^{\text{ref}}\right)$.

The off-diagonal elements of $\boldsymbol{J}_{\Gamma/\text{f}}$ have the form $\frac{\partial \Gamma_{\boldsymbol{k},i}}{\partial f_{p,\boldsymbol{l}}}$ with $\boldsymbol{k} \neq \boldsymbol{l}$, where $\boldsymbol{k}$ represents the encoding vector in k-space and $\boldsymbol{l}$ represents the spatial frequency of the property map, which is also a vector in the same k-space.

Because f_0 and f_1 are heavily coupled, it only makes sense to jointly calculate the partial derivative to these (i.e., to calculate $\left[\frac{\partial \Gamma_{\boldsymbol{k},i}}{\partial f_{0,\boldsymbol{l}}} \; \frac{\partial \Gamma_{\boldsymbol{k},i}}{\partial f_{1,\boldsymbol{l}}}\right]$). Because this derivative is formed via all of the values $u_{0,\boldsymbol{r}}$ and $u_{1,\boldsymbol{r}}$, we have

$$\left[\frac{\partial \Gamma_{\boldsymbol{k},i}}{\partial f_{0,\boldsymbol{l}}} \; \frac{\partial \Gamma_{\boldsymbol{k},i}}{\partial f_{1,\boldsymbol{l}}}\right] = \sum\nolimits_{\boldsymbol{r}} \left(\left[\frac{\partial \Gamma_{\boldsymbol{k},i}}{\partial u_{0,\boldsymbol{r}}} \; \frac{\partial \Gamma_{\boldsymbol{k},i}}{\partial u_{1,\boldsymbol{r}}}\right] \begin{bmatrix} \frac{\partial f_{0,\boldsymbol{l}}}{\partial u_{0,\boldsymbol{r}}} & \frac{\partial f_{0,\boldsymbol{l}}}{\partial u_{1,\boldsymbol{r}}} \\ \frac{\partial f_{1,\boldsymbol{l}}}{\partial u_{0,\boldsymbol{r}}} & \frac{\partial f_{1,\boldsymbol{l}}}{\partial u_{1,\boldsymbol{r}}} \end{bmatrix}^{-1} \right)$$

Now expanding to the second-order term of G:

$$G_{(\boldsymbol{k},\,i)}(u_{1,\boldsymbol{r}}) \approx g_{0,(\boldsymbol{k},\,i)} + \frac{\partial G_{(\boldsymbol{k},\,i)}}{\partial u_{1,\boldsymbol{r}}}\big|_{\boldsymbol{u}=\boldsymbol{u}^{\text{ref}}} \left(u_{1,\boldsymbol{r}} - u_1^{\text{ref}}\right) + \frac{\partial^2 G_{(\boldsymbol{k},\,i)}}{\partial u_{1,\boldsymbol{r}}^2}\big|_{\boldsymbol{u}=\boldsymbol{u}^{\text{ref}}} \left(u_{1,\boldsymbol{r}} - u_1^{\text{ref}}\right)^2$$

Using the relation $\Gamma_{\boldsymbol{k},i} = \sum_{\boldsymbol{r}} u_{0,\boldsymbol{r}} G_{(\boldsymbol{k},\, i)}\left(u_{1,\boldsymbol{r}}, \ldots, u_{(N_p-1),\boldsymbol{r}}\right) e^{i2\pi \boldsymbol{k}\boldsymbol{r}}$, we can write $\Gamma_{\boldsymbol{k},i} \approx \Gamma_{\boldsymbol{k},i,(1)} + \sum_{\boldsymbol{r}} \left(e^{i2\pi \boldsymbol{k}\boldsymbol{r}} u_{0,\boldsymbol{r}} q_{11,\boldsymbol{k},i} \left(\frac{u_{1,\boldsymbol{r}} - u_1^{\text{ref}}}{u_{1,\text{ref}}} \right)^2 \right)$, where $\Gamma_{\boldsymbol{k},i,(1)}$ is the first-order Taylor expansion and $q_{11,\boldsymbol{k},i}$ is shorthand for $u_{1,\text{ref}}^2 \frac{\partial^2 G_{(\boldsymbol{k},\, i)}}{\partial u_{1,\boldsymbol{r}}^2}\Big|_{\boldsymbol{u}=\boldsymbol{u}^{\text{ref}}}$, in analogy to $w_{p,\boldsymbol{k},i}$ (but with a "q" for "quadratic", referring to second order).

We wish to calculate $\begin{bmatrix} \frac{\partial \Gamma_{\boldsymbol{k},i}}{\partial f_{0,\boldsymbol{l}}} & \frac{\partial \Gamma_{\boldsymbol{k},i}}{\partial f_{1,\boldsymbol{l}}} \end{bmatrix}$, for which we need $\frac{\partial \Gamma_{\boldsymbol{k},i}}{\partial u_{0,\boldsymbol{r}}}$ and $\frac{\partial \Gamma_{\boldsymbol{k},i}}{\partial u_{1,\boldsymbol{r}}}$. It has already been established that the first-order terms thereof are zero if $\boldsymbol{k} \neq \boldsymbol{l}$. For the second-order terms of $\frac{\partial \Gamma_{\boldsymbol{k},i}}{\partial u_{0,\boldsymbol{r}}}$ and $\frac{\partial \Gamma_{\boldsymbol{k},i}}{\partial u_{1,\boldsymbol{r}}}$, we calculate

$$\begin{bmatrix} \frac{\partial \sum_{\boldsymbol{r}} \left(e^{i2\pi \boldsymbol{k}\cdot\boldsymbol{r}} u_{0,\boldsymbol{r}} q_{11,\boldsymbol{k},i} \left(\frac{u_{1,\boldsymbol{r}} - u_1^{\text{ref}}}{u_{1,\text{ref}}} \right)^2 \right)}{\partial u_{0,\boldsymbol{r}}} \\ \frac{\partial \sum_{\boldsymbol{r}} \left(e^{2\pi j \boldsymbol{k}\cdot\boldsymbol{r}} u_{0,\boldsymbol{r}} q_{11,\boldsymbol{k},i} \left(\frac{u_{1,\boldsymbol{r}} - u_1^{\text{ref}}}{u_{1,\text{ref}}} \right)^2 \right)}{\partial u_{1,\boldsymbol{r}}} \end{bmatrix}^T = \begin{bmatrix} q_{11,\boldsymbol{k},i} e^{2\pi j \boldsymbol{k}\cdot\boldsymbol{r}} \left(\frac{u_{1,\boldsymbol{r}} - u_1^{\text{ref}}}{u_1^{\text{ref}}} \right)^2 \\ \frac{2}{u_1^{\text{ref}}} q_{11,\boldsymbol{k},i} e^{2\pi j \boldsymbol{k}\cdot\boldsymbol{r}} u_{0,\boldsymbol{r}} \left(\frac{u_{1,\boldsymbol{r}} - u_1^{\text{ref}}}{u_1^{\text{ref}}} \right) \end{bmatrix}^T$$

In addition, we need $\begin{bmatrix} \frac{\partial f_{0,\boldsymbol{l}}}{\partial u_{0,\boldsymbol{r}}} & \frac{\partial f_{0,\boldsymbol{l}}}{\partial u_{1,\boldsymbol{r}}} \\ \frac{\partial f_{1,\boldsymbol{l}}}{\partial u_{0,\boldsymbol{r}}} & \frac{\partial f_{1,\boldsymbol{l}}}{\partial u_{1,\boldsymbol{r}}} \end{bmatrix}$.

Using the definitions of $f_{0,\boldsymbol{l}} = \sum_{\boldsymbol{r}} e^{i2\pi \boldsymbol{l}\cdot\boldsymbol{r}} u_{0,\boldsymbol{r}}$ and $f_{1,\boldsymbol{l}} = \sum_{\boldsymbol{r}} e^{i2\pi \boldsymbol{l}\cdot\boldsymbol{r}} u_{0,\boldsymbol{r}} \left(\frac{u_{1,\boldsymbol{r}} - u_1^{\text{ref}}}{u_{1,\boldsymbol{r}}} \right)$, we get $\frac{\partial f_{0,\boldsymbol{l}}}{\partial u_{0,\boldsymbol{r}}} = e^{i2\pi \boldsymbol{l}\cdot\boldsymbol{r}}$, $\frac{\partial f_{0,\boldsymbol{l}}}{\partial u_{1,\boldsymbol{r}}} = 0$, $\frac{\partial f_{1,\boldsymbol{l}}}{\partial u_{0,\boldsymbol{r}}} = e^{i2\pi \boldsymbol{l}\cdot\boldsymbol{r}} \frac{u_{1,\boldsymbol{r}}}{u_1^{\text{ref}}}$, and $\frac{\partial f_{1,\boldsymbol{l}}}{\partial u_{1,\boldsymbol{r}}} = e^{i2\pi \boldsymbol{l}\cdot\boldsymbol{r}} \frac{u_{0,\boldsymbol{r}}}{u_1^{\text{ref}}}$. (Note the common factor $e^{i2\pi \boldsymbol{l}\cdot\boldsymbol{r}}$ in the above.)

$$\begin{aligned} \text{Together, } \begin{bmatrix} \frac{\partial \Gamma_{\boldsymbol{k},i}}{\partial f_{0,\boldsymbol{l}}} \\ \frac{\partial \Gamma_{\boldsymbol{k},i}}{\partial f_{1,\boldsymbol{l}}} \end{bmatrix}^T \Big|_{\text{2nd order}} &= \sum_{\boldsymbol{r}} \left(\begin{bmatrix} q_{11,\boldsymbol{k},i} e^{i2\pi \boldsymbol{k}\cdot\boldsymbol{r}} \left(\frac{u_{1,\boldsymbol{r}} - u_1^{\text{ref}}}{u_1^{\text{ref}}} \right)^2 \\ \frac{2}{u_1^{\text{ref}}} q_{11,\boldsymbol{k},i} e^{i2\pi \boldsymbol{k}\cdot\boldsymbol{r}} u_{0,\boldsymbol{r}} \left(\frac{u_{1,\boldsymbol{r}} - u_1^{\text{ref}}}{u_1^{\text{ref}}} \right) \end{bmatrix}^T \begin{bmatrix} \frac{\partial f_{0,\boldsymbol{l}}}{\partial u_{0,\boldsymbol{r}}} & \frac{\partial f_{0,\boldsymbol{l}}}{\partial u_{1,\boldsymbol{r}}} \\ \frac{\partial f_{1,\boldsymbol{l}}}{\partial u_{0,\boldsymbol{r}}} & \frac{\partial f_{1,\boldsymbol{l}}}{\partial u_{1,\boldsymbol{r}}} \end{bmatrix}^{-1} \right) \\ &= \sum_{\boldsymbol{r}} \left(\begin{bmatrix} q_{11,\boldsymbol{k},i} e^{i2\pi \boldsymbol{k}\cdot\boldsymbol{r}} \left(\frac{u_{1,\boldsymbol{r}} - u_1^{\text{ref}}}{u_1^{\text{ref}}} \right)^2 \\ \frac{2}{u_1^{\text{ref}}} q_{11,\boldsymbol{k},i} e^{i2\pi \boldsymbol{k}\cdot\boldsymbol{r}} u_{0,\boldsymbol{r}} \left(\frac{u_{1,\boldsymbol{r}} - u_1^{\text{ref}}}{u_1^{\text{ref}}} \right) \end{bmatrix}^T \begin{bmatrix} \frac{\partial f_{0,\boldsymbol{l}}}{\partial u_{0,\boldsymbol{r}}} & \frac{\partial f_{0,\boldsymbol{l}}}{\partial u_{1,\boldsymbol{r}}} \\ \frac{\partial f_{1,\boldsymbol{l}}}{\partial u_{0,\boldsymbol{r}}} & \frac{\partial f_{1,\boldsymbol{l}}}{\partial u_{1,\boldsymbol{r}}} \end{bmatrix}^{-1} \right) \\ &= \sum_{\boldsymbol{r}} \left(e^{i2\pi (\boldsymbol{k}-\boldsymbol{l})\cdot\boldsymbol{r}} q_{11,\boldsymbol{k},i} \begin{bmatrix} \left(\frac{u_{1,\boldsymbol{r}} - u_1^{\text{ref}}}{u_1^{\text{ref}}} \right)^2 - 2 \left(\frac{u_{1,\boldsymbol{r}} - u_1^{\text{ref}}}{u_1^{\text{ref}}} \right) \\ 2 \left(\frac{u_{1,\boldsymbol{r}} - u_1^{\text{ref}}}{u_1^{\text{ref}}} \right) \end{bmatrix}^T \right) \end{aligned}$$

Taking the second element, $\frac{\partial \Gamma_{\boldsymbol{k},i}}{\partial f_{1,\boldsymbol{l}}}$, as an example, we get for its second-order Taylor term:

$$2 q_{11,\boldsymbol{k},i} \sum_{\boldsymbol{r}} \left(e^{i2\pi (\boldsymbol{k}-\boldsymbol{l})\cdot\boldsymbol{r}} \left(\frac{u_{1,\boldsymbol{r}} - u_1^{\text{ref}}}{u_1^{\text{ref}}} \right) \right),$$

which is the Fourier transform of the spatial pattern $\left(\frac{u_{1,\boldsymbol{r}} - u_1^{\text{ref}}}{u_1^{\text{ref}}} \right)$, evaluated at k-space position $\boldsymbol{k} - \boldsymbol{l}$. Given the knowledge that such a spatial pattern exhibits strong correlation among neighboring voxels (like in, e.g., T1-weighted MR images), the influence of that higher-order k-space term can be expected to quickly decrease when considering off-diagonal components in the $\boldsymbol{J}_{\Gamma/f}$ matrix (i.e., with increasing values of $|\boldsymbol{k} - \boldsymbol{l}|$).

APPENDIX C.

C.1 | THE CASE OF REAL-VALUED PROPERTIES AND CORRESPONDING SYMMETRY IN K-SPACE

In MRI, the data $d_{\boldsymbol{k},i}$ (modeled by $\Gamma_{\boldsymbol{k},i}$) are assumed to be complex. The unknowns $\boldsymbol{u}$ are obtained by a large-scale nonlinear inversion of the set of equations

$$\Gamma_{\boldsymbol{k},i} = \sum_{\boldsymbol{r}} u_{0,\boldsymbol{r}} G_{(\boldsymbol{k},\, i)}\left(u_{1,\boldsymbol{r}}, \ldots, u_{(N_p-1),\boldsymbol{r}}\right) e^{i2\pi \boldsymbol{k}\cdot\boldsymbol{r}}.$$

An unconstrained solution of this inversion problem would lead to complex values of the unknowns $u_{p,\boldsymbol{r}}$. Yet, many properties (e.g., the relaxation time T_1) are known to be real quantities.

Without loss of generality, we here consider all unknowns to be real. This has an impact on the structure of the Jacobian $\boldsymbol{J}_{\Gamma/f} = \left[\frac{\partial \Gamma_{\boldsymbol{k},i}}{\partial f_{p,\boldsymbol{l}}} \right]$, because we now have a constraint on f. Given the relation between u and f, as specified in Equation (2), the assumption of a real-valued u implies that

$f_{p,\boldsymbol{k}} = f^*_{p,-\boldsymbol{k}}$. This reduces the number of (complex) unknowns (e.g., by considering only positive values of $\boldsymbol{k}$ for the unknowns). Consequently, the number of columns in the Jacobian reduces to roughly $N_p N_k/2$ (see sequel). The data, however, may still be available for all positive and negative values of $\boldsymbol{k}$.

This symmetry implies a slight modification of the forward model of Equation (A6), which is reformulated as

$$\Gamma_{\boldsymbol{k},i} \approx \begin{cases} \sum_{p=0}^{N_p-1} w_{p,\boldsymbol{k},i} \cdot f_{p,\boldsymbol{k}} & k_y \geq 0 \\ \sum_{p=0}^{N_p-1} w_{p,\boldsymbol{k},i} \cdot f^*_{p,-\boldsymbol{k}} & k_y < 0 \end{cases}.$$

(Here, the symmetry plane has been taken perpendicular to k_y; in principle, any other plane through $\boldsymbol{k} = 0$ could be taken). We make use of an auxiliary variable

$$\begin{aligned} \Gamma'_{\boldsymbol{k},\mathrm{i}} &= \Gamma_{\boldsymbol{k},i} \quad k_y \geq 0 \\ \Gamma'_{\boldsymbol{k},(i+N_{\mathrm{instances}})} &= \Gamma^*_{\boldsymbol{k},i} \quad k_y < 0 \end{aligned}$$

and we rearrange the vector $\boldsymbol{\Gamma}'$ such that positive and negative k_y-indices are adjacent.

With this reformulation, and assuming a symmetric range of sampled encodings $\boldsymbol{k}$, the matrix $\boldsymbol{J}_{\Gamma'/\mathrm{f}}$ consists of $n = \mathrm{ceil}((N_k+1)/2)$ nonzero blocks of size $2N_{\mathrm{instances}} \times N_p$ blocks having content $\begin{bmatrix} w_{p,\boldsymbol{k},i} \\ w^*_{p,-\boldsymbol{k},i} \end{bmatrix}$ (except for the outmost k-values and for $\boldsymbol{k} = 0$).

The Fisher Information Matrix thereby has n nonzero blocks of size $N_p \times N_p$.

This modification leads to better estimates of the noise (results not shown) compared with a block-diagonal Jacobian $\boldsymbol{J}_{\Gamma'/\mathrm{f}}$ where the k-space symmetry is ignored.